

**THERMAL STABILITY ENHANCEMENT OF
MAPBI₃ FILM BY INCORPORATING
POLY(METHYL METHACRYLATE)
ADDITIVES AND ENCAPSULATION
LAYERS FOR PEROVSKITE SOLAR CELL
APPLICATION**

CHUO SING ERN

UNIVERSITI TUNKU ABDUL RAHMAN

**THERMAL STABILITY ENHANCEMENT OF MAPBI₃ FILM BY
INCORPORATING POLY(METHYL METHACRYLATE) ADDITIVES
AND ENCAPSULATION LAYERS FOR PEROVSKITE SOLAR CELL
APPLICATION**

CHUO SING ERN


**A project report submitted in partial fulfilment of the
requirements for the award of Bachelor of Engineering
(Honours) Mechanical Engineering**

**Lee Kong Chian Faculty of Engineering and Science
Universiti Tunku Abdul Rahman**

May 2023

DECLARATION

I hereby declare that this project report is based on my original work except for citations and quotations which have been duly acknowledged. I also declare that it has not been previously and concurrently submitted for any other degree or award at UTAR or other institutions.

Signature : 

Name : Chuo Sing Ern

ID No. : 1802724

Date : 20/5/2023

APPROVAL FOR SUBMISSION

I certify that this project report entitled **“THERMAL STABILITY ENHANCEMENT OF MAPBI₃ FILM BY INCORPORATING POLY(METHYL METHACRYLATE) ADDITIVES AND ENCAPSULATION LAYERS FOR PEROVSKITE SOLAR CELL APPLICATION”** was prepared by **CHUO SING ERN** has met the required standard for submission in partial fulfilment of the requirements for the award of Bachelor of Engineering (Honours) Mechanical Engineering at Universiti Tunku Abdul Rahman.

Approved by,

Signature : *chaiy*

Supervisor : Dr. Ng Chai Yan

Date : 20/5/2023

Signature : *junhke*

Co-Supervisor : Dr. Jun Hieng Kiat

Date : 20/5/2023

The copyright of this report belongs to the author under the terms of the copyright Act 1987 as qualified by Intellectual Property Policy of Universiti Tunku Abdul Rahman. Due acknowledgement shall always be made of the use of any material contained in, or derived from, this report.

© 2023, Chuo Sing Ern. All right reserved.

ACKNOWLEDGEMENTS

I would like to thank everyone who had contributed to the successful completion of this project. I would like to express my gratitude to my research supervisor, Dr. Ng Chai Yan and my co-supervisor Dr. Jun Hieng Kiat for their invaluable advice, guidance and her enormous patience throughout the development of the research.

In addition, I would also like to express my gratitude to Soo Yew Hang, a PhD student which specialized in the field of perovskite solar cells, for guiding me throughout the whole experiment. Furthermore, I would also like to express my gratitude to my loving parents and friends who had helped and given me encouragement so that I may persist with utmost effort throughout this entire project. Last but not least, I would also like to thank the lab staffs especially Ms. Suzana for helping me with my SEM and XRD analyses so that I may operate the equipment without any errors.

ABSTRACT

Perovskite solar cells (PSCs) are just like conventional solar cells with the exception of a perovskite material acting as its light absorbing layer, which converts solar energy to electrical energy. Due to the popularity of methylammonium lead iodide (MAPbI₃) being used as a light-absorbing layer for PSCs, this study was conducted with the focus on PSCs containing MAPbI₃. The successful deposition of metal oxide sol, which is low in cost, above the perovskite layer will lead to the commercialization of PSCs that utilizes metal oxides as its charge transport layers (CTL) which are both operationally stable and economic. In regards, post-annealing at around 150 °C is needed to deposit metal oxide sols above the perovskite layer. However, the weak thermal stability of MAPbI₃ that lies underneath the metal oxide sol does not tolerate such heat and will thermally degrade, resulting in the loss of functionality of the device. In this work, PMMA was added as additives and as dual encapsulation layers to enhance the thermal stability of MAPbI₃ films using vacuum-assisted solution processing (VASP) and antisolvent method. The results showed that 0.15 wt% of PMMA additives was the most prominent amount in enhancing the thermal stability of MAPbI₃ films whereby a significant reduction in XRD peak intensity ratio of PbI₂ to MAPbI₃ was observed after 5 hours of thermal stressing. In this context, the peak intensity ratios of 8.6618 and 1.7577 were exhibited for pristine samples and 0.15 wt% PMMA-incorporated samples, respectively. Besides that, the peak intensity ratios of 1.0936 and 2.4087 were exhibited for dual and single-PMMA encapsulated samples, respectively. The lower peak intensity ratio of PbI₂ to MAPbI₃ signified lesser thermal degradation of MAPbI₃ to PbI₂. Apart from that, the lower formation of PbI₂ needle grains and the retention of MAPbI₃ UV-Vis band edge were observed for both 0.15 wt% PMMA-incorporated and dual PMMA-encapsulated samples. The thermal stability enhancement effects of both the incorporation of PMMA additives and dual PMMA encapsulation layers can be explained through the passivation of grain boundary defects at the film/air interface and within the MAPbI₃ films. With this discovery, operationally stable and economic PSCs with higher

thermal stability that allows the deposition of metal oxide sols as its CTLs may be developed.

TABLE OF CONTENTS

DECLARATION	i
APPROVAL FOR SUBMISSION	ii
ACKNOWLEDGEMENTS	iv
ABSTRACT	v
TABLE OF CONTENTS	vii
LIST OF TABLES	xi
LIST OF FIGURES	xii
LIST OF SYMBOLS / ABBREVIATIONS	xvi

CHAPTER

1	INTRODUCTION	17
	1.1 General Introduction	17
	1.2 Importance of the Study	18
	1.3 Problem Statement	18
	1.4 Aim and Objectives	19
	1.5 Scope and Limitation of the Study	19
	1.6 Contribution of the Study	20
	1.7 Outline of the Report	20
2	LITERATURE REVIEW	22
	2.1 Introduction	22
	2.2 Background of PSC	22
	2.2.1 Working Principles of PSC	23
	2.2.2 Commercialization Problem of PSC	26
	2.3 Structure of PSC	27
	2.3.1 Organic CTLs	29
	2.3.2 Inorganic CTLs	30
	2.4 Stability of MAPbI ₃ Layer	33

2.4.1	Moisture Stability	33
2.4.2	Oxygen Stability	34
2.4.3	Thermal Stability	34
2.4.4	Thermal Stability Enhancement of MAPbI ₃ Film by PMMA Encapsulation	36
2.4.5	Thermal Stability Enhancement of MAPbI ₃ Film Through Incorporation of PMMA Additives	39
2.5	Summary	44
3	METHODOLOGY AND WORK PLAN	45
3.1	Introduction	45
3.2	Spin-coating of SnO ₂ Solution on the Fluorine-Doped Tin Oxide (FTO) Glass Pieces	46
3.3	Methodology for MAPbI ₃ Films with Incorporation of PMMA Additives Using VASP	46
3.3.1	Preparation of MAPbI ₃ Precursor Solution with the Addition of PMMA	47
3.3.2	Preparation of PMMA Solution	47
3.3.3	Deposition of PMMA-MAPbI ₃ and PMMA Encapsulation Layer	48
3.3.4	Characterizations	49
3.4	Methodology for MAPbI ₃ Films with Incorporation of PMMA Additives Using Antisolvent Method	49
3.4.1	Preparation of MAPbI ₃ Precursor Solution with the Addition of PMMA	50
3.4.2	Deposition of PMMA-MAPbI ₃ and PMMA Encapsulation Layer	50
3.4.3	Characterizations	51
3.5	Methodology for MAPbI ₃ Films with Dual PMMA Encapsulation Layers	51
3.5.1	Preparation of MAPbI ₃ Precursor Solution	51

	3.5.2 Preparation of Second PMMA Solution for Dual PMMA Encapsulation	52
	3.5.3 Deposition of MAPbI ₃ and Dual PMMA Encapsulation Layers	52
	3.5.4 Characterizations	53
	3.6 Summary	53
4	RESULTS AND DISCUSSION	54
	4.1 Introduction	54
	4.2 PMMA-Encapsulated Samples Incorporated with PMMA Additives with Vacuum-Assisted Solution Process (VASP) and Antisolvent Method	54
	4.2.1 Physical Appearance Analysis of PMMA-Encapsulated Samples Incorporated with PMMA Additives with VASP and Antisolvent Method	55
	4.2.2 XRD Analysis of PMMA-Encapsulated Samples Incorporated with PMMA Additives with Antisolvent Method	59
	4.3 Pristine Samples with Single and Dual PMMA Encapsulation Layers	65
	4.3.1 Physical Appearance Analysis of Pristine Samples with Single and Dual PMMA Encapsulation Layers	66
	4.3.2 XRD Analysis of Pristine Samples with Single and Dual PMMA Encapsulation Layers	67
	4.3.3 UV-Vis Spectroscopy Analysis of Pristine Samples with Single and Dual PMMA Encapsulation Layers	70
	4.3.4 SEM Analysis of Pristine Samples with Single and Dual PMMA Encapsulation Layers	73
	4.4 Thermal Stability Enhancement Mechanism of PMMA As Additive and Dual Encapsulation Layers	76
	4.5 Summary	78

5	CONCLUSIONS AND RECOMMENDATIONS	80
5.1	Conclusions	80
5.2	Recommendations for Future Work	81
	REFERENCES	82

LIST OF TABLES

Table 4.1:	Peak Intensity Ratio of $\text{PbI}_2/\text{MAPbI}_3$ for Antisolvent Perovskite Samples.	65
Table 4.2:	Peak Intensity Ratio of $\text{PbI}_2/\text{MAPbI}_3$ for Single and Dual PMMA-Encapsulated Perovskite Samples.	70
Table 4.3:	Average Grain Size of S-PMMA- MAPbI_3 and D-PMMA- MAPbI_3 Films Annealed at Various Hours.	76

LIST OF FIGURES

Figure 2.1:	Perovskite Structure of MAPbI ₃ (Boix, Nonomura, Mathews and Mhaisalkar, 2014).	22
Figure 2.2:	Efficiency of PSCs Against Aperture Area In 2020 (Wu et al., 2021).	27
Figure 2.3:	N-i-p and P-i-n Structure of PSC.	28
Figure 2.4:	Colour Variation of HOOC–Ph–SH/Perovskite/Spiro-OMeTAD and HOOC–Ph–SH/Perovskite/HS–PhF ₅ /Spiro-OMeTAD Films (Cao et al., 2015).	33
Figure 2.5:	SEM Images of ITO/TiO ₂ /Perovskite Samples in Pristine and N ₂ Atmospheres at 85 °C For 24 Hours (Conings et al., 2015).	35
Figure 2.6:	Thermal Degradation Comparison of MAPbI ₃ and FAPbI ₃ When Heated at 150 °C (Eperon et al., 2014).	35
Figure 2.7:	XRD Results of Control and PMMA-Encapsulated MAPbI ₃ Films at 150 °C at Different Periods (Soo et al., 2021).	36
Figure 2.8:	Physical Appearances of Annealed MAPbI ₃ Films with Both PMMA-Encapsulated and Unencapsulated Portion at Various Durations (Soo et al., 2021).	37
Figure 2.9:	Passivation Mechanism on GBs by Carbonyl Group of PMMA (Soo et al., 2021).	39
Figure 2.10:	XRD Patterns Between PMMA-Encapsulated MAPbI ₃ Films with and Without the Addition of Caffeine When Annealed At 150 °C for Various Hours (Soo et al., 2022).	40
Figure 2.11:	Passivation Mechanism of Caffeine at GBs Within MAPbI ₃ Film (Soo et al., 2022).	41
Figure 2.12:	FTIR Spectra of PMMA-PbI ₂ Mixture and Pristine PMMA Films (Bi et al., 2016).	42
Figure 2.13:	Cross-Sectional SEM Results of Perovskite Films with Various Concentrations of PMMA Added (Bi et al., 2016).	42

Figure 2.14:	Normalized PCEs with the Initial PCE After Annealing at 100 °C As a Function of PCBM Added (Park et al., 2017).	43
Figure 3.1:	Sample Structures: (a) VASP and Antisolvent Method, (b) Single and Dual PMMA Encapsulation.	45
Figure 3.2:	Illustration for Spin-coating of SnO ₂ onto FTO Glass.	46
Figure 3.3:	Illustration for Preparation of MAPbI ₃ Precursor Solution with the Addition of PMMA Additives.	47
Figure 3.4:	Illustration for the Preparation of PMMA Solution.	48
Figure 3.5:	Illustration for Deposition of PMMA-MAPbI ₃ Using VASP.	49
Figure 3.6:	Illustration for Deposition of PMMA-MAPbI ₃ Using Antisolvent.	51
Figure 4.1:	Pristine Samples with VASP Annealed at 150 °C for Various Hours.	55
Figure 4.2:	Samples Incorporated with 1 mg of PMMA Additives with VASP Annealed at 150 °C for Various Hours.	55
Figure 4.3:	Samples Incorporated with 3 mg of PMMA Additives with VASP Annealed at 150 °C for Various Hours.	55
Figure 4.4:	Samples Incorporated with 5 mg of PMMA Additives with VASP Annealed at 150 °C for Various Hours.	56
Figure 4.5:	Samples Incorporated with 7 mg of PMMA Additives with VASP Annealed at 150 °C for Various Hours.	56
Figure 4.6:	Suspension of White Floccule in the Perovskite Precursor Solution (Jia et al., 2017).	57
Figure 4.7:	Pristine Samples with Antisolvent Method Annealed at 150 °C for Various Hours.	58
Figure 4.8:	Samples Incorporated with 0.05 wt% of PMMA Additives with Antisolvent Method Annealed at 150 °C for Various Hours.	59
Figure 4.9:	Samples Incorporated with 0.10 wt% of PMMA Additives with Antisolvent Method Annealed at 150 °C for Various Hours.	59

Figure 4.10:	Samples Incorporated with 0.15 wt% of PMMA Additives with Antisolvent Method Annealed at 150 °C for Various Hours.	59
Figure 4.11:	XRD Patterns of Pristine PMMA-Encapsulated MAPbI ₃ Films using Antisolvent Method Annealed for Various Times.	60
Figure 4.12:	XRD Patterns of PMMA-Encapsulated MAPbI ₃ Films Incorporated with 0.05 wt% of PMMA using Antisolvent Method Annealed for Various Times.	60
Figure 4.13:	XRD Patterns of PMMA-Encapsulated MAPbI ₃ Films Incorporated with 0.10 wt% of PMMA using Antisolvent Method Annealed for Various Times.	61
Figure 4.14:	XRD Patterns of PMMA-Encapsulated MAPbI ₃ Films Incorporated with 0.15 wt% of PMMA using Antisolvent Method Annealed for Various Times.	61
Figure 4.15:	The Annealing Time and Temperature on the Colour Transition of the Perovskite Films with and Without PMMA (Jia et al., 2017).	62
Figure 4.16:	XRD Patterns of Perovskite Films with PMMA Evolved with Annealing Time (Jia et al., 2017).	63
Figure 4.17:	Physical Appearance of S-PMMA-MAPbI ₃ Films Annealed at 150 °C for Various Hours.	66
Figure 4.18:	Physical Appearance of D-PMMA-MAPbI ₃ Films Annealed at 150 °C for Various Hours.	66
Figure 4.19:	XRD Patterns of S-PMMA-MAPbI ₃ Films Using VASP Method Annealed at 150 °C for Various Hours.	68
Figure 4.20:	XRD Patterns of D-PMMA-MAPbI ₃ Films Using VASP Method Annealed at 150 °C for Various Hours.	68
Figure 4.21:	UV-Vis Spectra of S-PMMA-MAPbI ₃ Films.	71
Figure 4.22:	UV-Vis Spectra of D-PMMA-MAPbI ₃ Films.	71
Figure 4.23:	UV-Vis Absorption Spectra of Pristine MAPbI ₃ , Pure PbI ₂ and Degraded MAPbI ₃ Film (Yang et al., 2015).	72
Figure 4.24:	SEM Images of S-PMMA-MAPbI ₃ Film Annealed for Various Times: (a) Control, (b) 1 h, (c) 2 h, (d) 3 h, (e) 5 h and (f) 5 h (Lower Magnification).	73

- Figure 4.25: SEM Images of D-PMMA-MAPbI₃ Film Annealed for Various Times: (a) Control, (b) 1 h, (c) 2 h, (d) 3 h, (e) 5 h and (f) 5 h (Lower Magnification). 74
- Figure 4.26: Illustration of Ostwald Recrystallization (Huang et al., 2018). 75
- Figure 4.27: Passivation Mechanism on GBs by Dual PMMA Encapsulation Layers Through the Carbonyl Group of PMMA. 77
- Figure 4.28: Passivation Mechanism on GBs by PMMA Additives Within MAPbI₃ Films. 78

LIST OF SYMBOLS / ABBREVIATIONS

<i>FF</i>	fill factor
<i>J_{sc}</i>	short circuit current, mA
<i>V_{oc}</i>	open circuit voltage, V
3-D	three-dimensional
ALD	atomic layer deposition
AM	air mass
CSSC	commercialized silicon solar cells
CTL	charge transport layer
DMF	dimethylformamide
DMSO	dimethyl sulfoxide
DSC	dye-sensitized solar cell
ETL	electron transport layer
FTIR	fourier transform infrared spectroscopy
FTO	fluorine-doped tin oxide
GB	grain boundary
HTL	hole transport layer
NP	nanoparticle
PCE	power conversion efficiency
PVD	physical vapour deposition
PSC	perovskite solar cell
PTNG	polymer-templated nucleation and growth
SEM	scanning electron microscopy
TCO	transparent conductive oxide
UV-Vis	ultraviolet-visible
VASP	vacuum-assisted solution processing
XRD	x-ray diffraction

CHAPTER 1

INTRODUCTION

1.1 General Introduction

With the ever-growing usage of energy all around the world, it is undeniable that the need for exploiting renewable energy sources has become trivial throughout the world. With solar energy being one of the main renewable energies, technological advancements have created solar cells that function by converting sunlight into electricity (Mohammad Bagher, 2015).

A recent prediction predicts that photovoltaics will contribute to about a third of new energy generation capacity globally between now and 2030, thanks to recent significant decreases in the manufacturing costs of conventional silicon solar cell technology. In the field of microelectronics, silicon possesses several advantages that have made it challenging to replace as the preferred solar material. However, opportunities are presented to technologies that offer either noticeably improved energy conversion efficiency or significantly lower processing costs. In regards, perovskite solar cells (PSC) are currently being developed and studied due to their potential to offer tantalizing prospects on both fronts (Green, Ho-Baillie and Snaith, 2014).

Perovskites have 3D crystal structures with the stoichiometry of ABX_3 . Miyasaka and his colleagues were the first to report the use of perovskite in producing photovoltaic results whereby they adopted hybrid perovskite compounds by developing methylammonium lead bromide ($MAPbBr_3$) solar cells that achieved a power conversion efficiency (PCE) of 2.2 %. Later on in the year 2009, the replacement of bromine with iodine was able to improve the PCE to 3.8 % (Kojima et al., 2007; Kojima et al., 2009). By changing materials composition, device architectures and processing conditions, studies have shown the record of producing PSCs that are capable of achieving PCE of beyond 20 % (Snaith, 2018). Due to the popularity of methylammonium lead iodide ($MAPbI_3$) being used as a light-absorbing layer for PSCs, this study was conducted with the focus on PSCs containing $MAPbI_3$.

1.2 Importance of the Study

The results of this study may clarify whether poly(methyl methacrylate) (PMMA) additives and dual PMMA encapsulation layers will increase the thermal stability of the perovskite layer, namely, MAPbI₃ in this case. If so, this study also helps to offer a clearer explanation of the thermal stability strengthening effect of PMMA additives and encapsulation layers in the MAPbI₃ layer in terms of its mechanism and its potential contributions to the commercialization of PSC. By successfully identifying the mechanism behind the thermal stability strengthening effect, researchers can utilize the knowledge to implement long-term stability upon PSCs which remains as one of the largest obstacles towards the commercialization of PSCs.

1.3 Problem Statement

Recent studies have shown that PSCs can achieve PCEs of beyond 20 %. Nonetheless, the operational stability of PSCs still falls behind that of commercialized silicon solar cells (CSSC) which have an average lifespan of 20 to 30 years (Soo et al., 2022). Besides that, Rong et al. (2018) reported that PSCs successfully exhibited a lifespan of 10000 hours. However, such lifespan was only achieved under ultraviolet-filtered light which differs from practical situations whereby ultraviolet rays are always present in sunlight. Moreover, PSCs are faced with various stability issues resulting from exposure to moisture, oxygen, and elevated temperature. In contrast, CSSCs were able to maintain long-term operational stability despite being exposed to harsh outdoor conditions (Jordan and Kurtz, 2011). Thus, improvement must be made to achieve good operational stability of PSCs, starting from its thermal stability.

According to a previous report by Soo et al. (2022), the successful deposition of metal oxide sol, which is low in cost, above the perovskite layer will lead to the commercialization of PSCs that utilizes metal oxides as its charge transport layers (CTL) which are both operationally stable and economic. In regards, post-annealing at around 150 °C is needed to deposit metal oxide sols above the perovskite layer. However, the weak thermal stability of MAPbI₃ that lies underneath the metal oxide sol does not tolerate such heat and will thermally degrade, resulting in the loss of functionality of the device. Although PMMA has been reported by Soo et al. (2021) to be used as a single encapsulation layer

for MAPbI₃ film to reduce thermal degradation, the working mechanism behind PMMA as an additive and as dual encapsulation layers for the strengthening of thermal stability have not yet been explored.

1.4 Aim and Objectives

The main aim of this study is to investigate the ability and working mechanism of PMMA additives and encapsulation layers in improving the thermal stability of MAPbI₃ film for PSC application. Besides that, the specific objectives of this research are:

- i. To compare the thermal stability enhancement effects of MAPbI₃ film with and without PMMA additives.
- ii. To investigate the thermal stability enhancement effects of MAPbI₃ film with various amounts of PMMA additives.
- iii. To compare the thermal stability enhancement effects of MAPbI₃ film with single and dual PMMA encapsulation layers.
- iv. To examine the reaction mechanism of PMMA additives and encapsulation layers with MAPbI₃ film.

1.5 Scope and Limitation of the Study

The scope of the study is to investigate the thermal stability enhancement effect of PMMA when incorporated as an additive and as encapsulation layers in MAPbI₃ films. To further investigate the thermal stability strengthening effect, different amounts of PMMA additives were used for each set of experiments. The scope of the study is important to pave the way towards the commercialization of MAPbI₃ PSCs, the reason being that the annealing of metal oxide sol above the MAPbI₃ film will thermally degrade it. Although organic CTLs that do not require annealing could be utilized, the overall contribution towards commercialization is far lesser than the utilization of metal oxide sols, provided that the thermal stability issue could be mitigated. Thus, this study will focus on the enhancing the thermal stability of MAPbI₃ films for the utilization of inorganic CTLs which are represented by metal oxide sols in this case.

The limitations of the study include the lack of previous research studies regarding the effect of PMMA additives and dual PMMA encapsulation

layers on improving the thermal stability of MAPbI₃ film. Thus, the mechanisms behind the thermal degradation countering effect of PMMA additives and encapsulation layers are also vague. Besides that, this experiment will focus on utilizing spin-coating method to produce the MAPbI₃ films since it is cheaper and easier to perform when compared to other deposition methods. Thus, this limits the study area for this research to the usage of spin-coating only since the deposition method also affects the resulting properties of PSCs. Moreover, since most of the low-temperature metal oxide sols require annealing at less than or equal to 150 °C, the thermal stability investigation for this study is limited to applications of less than or equal to 150 °C only.

1.6 Contribution of the Study

This study investigates the thermal stability enhancement effects of both PMMA additives and dual PMMA encapsulation layers. In this context, by identifying the mechanism behind their thermal stability enhancement effects, developers can bring PSCs one step closer towards commercialization. This is because the weak thermal stability of the MAPbI₃ layer cannot tolerate the post-annealing of metal oxide sols above the perovskite layer as mentioned in Section 1.3. Therefore, by studying the mechanism behind the thermal stability enhancement effects of PMMA additives and dual PMMA encapsulation layers, higher operational stability and economic PSCs can be made available through the successful deposition of metal oxide sols as the CTLs for PSCs.

1.7 Outline of the Report

In this report, Chapter 1 introduces PSCs together with their potential to be commercialized by increasing their operational stability through the successful deposition of metal oxide sols as the CTLs for PSCs. Chapter 2 showcases some of the reviews made by previous researchers regarding the background of PSCs, the benefits of utilizing metal oxide sols at CTLs, and the stability of MAPbI₃ layer especially when exposed to heat. Besides that, Chapter 2 further reviews some of the past researchers' work on the thermal stability enhancement of MAPbI₃ films through the incorporation of additives such as PMMA, followed by the thermal stability enhancement effects of PMMA encapsulation. After that, Chapter 3 discusses how the experiment will be carried out to study the

objectives of this report. Chapter 4 then discusses the findings and results of the experiment through the use of various sample characterizations such as physical appearance assessment, X-ray diffraction (XRD), scanning electron microscopy (SEM) and ultraviolet-visible (UV-Vis) spectroscopy analysis. Last but not least, Chapter 5 discusses the conclusion of the study and recommendations for improvement in future works.

CHAPTER 2

LITERATURE REVIEW

2.1 Introduction

This chapter will discuss the background, structure, thermal stability issue and ways of enhancement for the MAPbI₃ film of PSC.

First off, the background will discuss the function and working principle of PSC, while at the same time investigating the problems for the commercialization of PSC. After that, the structure of the PSC will be discussed in detail regarding each of the separate layers that form the PSC. The different structures of PSC will also be discussed and compared in terms of their long-term operational stability and so on. Last but not least, the last part of the chapter will discuss the issue regarding the thermal stability of the MAPbI₃ film in PSC to identify the possibility for the commercialization of all-metal oxide CTL PSC in the future. Under the topic of thermal stability issues, different methods of enhancing the thermal stability of MAPbI₃ films such as PMMA encapsulation and incorporation of PMMA additives will be discussed in detail.

2.2 Background of PSC

As mentioned before, with the stoichiometry of ABX₃, three main ions are present in the 3-D crystal structure of perovskites. Generally, A is a large cation while B is a smaller metal cation followed by X being a halide anion (Boix et al., 2014; Snaith, 2018). Figure 2.1 shows the perovskite structure of MAPbI₃.

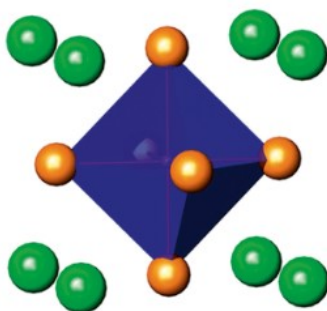


Figure 2.1: Perovskite Structure of MAPbI₃ (Boix, Nonomura, Mathews and Mhaisalkar, 2014).

Generally, the most commonly used light-absorbing layer in PSC is MAPbI₃ due to its benefits which include higher efficiency, ease of fabrication and lower cost of materials (Snaith, 2018). MAPbI₃ is a type of organic-inorganic halide perovskites, whereby the methylammonium can also be replaced by other organic cations such as ethylammonium and formamidinium. Besides that, the B cation can also be replaced by tin (Sn), however doing so will give rise to the lower stability of PSC as a result of the higher possibility of oxidation for Sn in iodide perovskite (Green, Ho-Baillie and Snaith, 2014). Furthermore, MASnI₃ offers a lower efficiency of 10.42 % when compared to MAPbI₃ with higher efficiency of 18.91 %. This difference in efficiency may be due to MAPbI₃ having a more favourable bandgap for light absorption (Marí-Guaita et al., 2022). For the X anion, it could be replaced by other halide ions such as bromide (Br) and chloride (Cl), or sometimes even in the form of mixed halides such as CH₃NH₃PbI_{3-x}Cl_x and CH₃NH₃PbI_{3-x}Br_x.

2.2.1 Working Principles of PSC

To commercialize the use of PSCs in the future market, various studies are conducted to identify the working principles with the focus on the parameters that define the efficiency of a photovoltaic cell. The parameters include the fill factor (FF), short circuit current (J_{SC}) and open circuit voltage (V_{OC}). To study the working principles of PSCs, the focus will be on the physical processes that govern these photovoltaic parameters, which include generation of charges, the transport of charges, recombination of charges, and the extraction of charges.

First of all, the superior light-absorbing properties and low binding energy of excitons for PSCs are two of its key traits, which characterize their distinctiveness and contribute to their success. Acting as a light absorber layer, a photon with energy greater than the bandgap of the active material of the perovskite film will excite the active material, producing an exciton. Metal halide perovskites such as MAPbI₃ have a high extinction coefficient of more than 10⁴ cm⁻¹, thus allowing incident light to be absorbed using a very thin perovskite layer (Yin, Shi and Yan, 2014). Besides that, the high optical absorption and tuneable bandgap properties of perovskite films have enabled the use of thinner films (Rhee, An and Kang, 2020). As a result, Yoshikawa et al. (2017) reported the use of an absorber layer within the range of 300–600 nm

which is thinner than silicon solar cells. Thinner films are better at absorbing light and providing less resistance for charge transport due to shorter paths. Moreover, thinner films also mean fewer opportunities for recombination, which lowers energy losses and raises the device's final voltage. Besides that, perovskites such as MAPbI_3 and MaPbBr_3 have high dielectric constant, meaning higher energy is needed to dissociate an exciton, thus explaining the reason for the low binding energy of excitons for perovskites which in turn results in a huge density of holes and electrons in the perovskite material.

To produce a high PCE, excellent charge transport properties are also needed. This can be observed in metal halide perovskites in regards to their long carrier diffusion lengths and long carrier lifetime of approximately $5 \mu\text{m}$ and $1 \mu\text{s}$ in single-crystal and polycrystalline films respectively (Shi et al., 2015; Nie et al., 2015). Unlike other photovoltaic devices, metal halide perovskites must offer their own effective electrons and holes transport. Besides that, Xing et al. (2013) stated that PSCs have well-balanced diffusion lengths for both electrons and holes with an approximate length of 100 nm , which are crucial for solar cells that are thin to successfully extract both carriers. Furthermore, since the PSC was initially a titanium dioxide (TiO_2)-sensitized cell, it was reasonable to assume that the major transport route for electrons would be into the wide bandgap metal oxide. PSCs can, however, function in a logically different configuration from dye-sensitized solar cells (DSC), as evidenced by the detection of considerable efficiencies in PSCs without electron transporting material, without hole transporting material, or even in thin-film form. These findings provide compelling evidence that in the metal halide perovskite absorber material, photogenerated electrons and holes coexist and go to the selective contacts, where they are individually collected (Gonzalez-Pedro et al., 2014).

The charge recombination mechanisms in PSCs can be separated into three ways, which include through shunt pathways that are directly contacted between hole transport layer (HTL) and electron transport layer (ETL), recombination within the bulk of perovskite film, and last but not least, recombination at the perovskite/HTL or perovskite/ETL interface (Marchioro et al., 2014). Back in the early days when the film fabrication techniques are still not well developed, the deposition of perovskite films were unable to ensure

perfect coverage of the whole surface of the material lying beneath it, thus leading to charge recombination due to the direct contact between HTL and ETL at the perovskite pinholes. Through various research and development of fabrication techniques, both planar and mesoporous perovskite devices can achieve complete coverage, thus boosting the PCE over 15 % while producing a V_{OC} of 1.1 V for MAPbI₃ films (Liu, Johnston and Snaith, 2013). This fact shows that charge recombination through shunt pathways is dependent on the architecture of the layers of PSCs. In contrast, bulk recombination, which can be either band-to-band radiative recombination or non-radiative trap-assisted recombination, explains how holes and electrons combine in the bulk of the perovskite. Thus, the traps that are present in the perovskite material will determine the bulk recombination process and the loss rates (Boix, Raga and Mathews, 2018). For interfacial recombination, Pockett and Carnie (2017) stated that there is a close relation between ionic movement and interfacial recombination in which both have been proposed to cause hysteresis. This statement is also supported by Calado et al. (2016) whereby it was stated that ionic movement occurs in all devices regardless of hysteresis, whereas hysteresis is only present when there are significant rates of interfacial recombination at the interface between the perovskite and the contact. Xiao et al. (2014) also presented that interfacial polarization due to ion or vacancy accumulation will directly influence the amount of interfacial recombination which is shown in the example of the giant switchable photovoltaic effect.

Lastly, the final mechanism would be charge extraction. The interfacial contacts of the PSC should be optimized in charge extraction to reduce voltage loss, current loss, and FF loss. To prevent a decrease in light intensity in the perovskite, a selective contact that does not absorb light would be deemed perfect. Besides that, any energetic losses during charge injection from the absorber should also be avoided, meaning no interfacial recombination. The series resistance of the selective contacts should also be reduced for good photovoltaic performance. However, any material in real life will induce losses in the final performance of photovoltaic cells, by affecting the photovoltaic parameters, namely J_{SC} , V_{OC} and FF. The J_{SC} may be affected by parasitic optical absorption, while V_{OC} and FF may be affected by interfacial

recombination losses, and resistance of the material during charge extraction respectively (Boix, Raga and Mathews, 2018). The initial PSCs that utilized liquid electrolyte to extract the holes from the absorber only reported a PCE of 3.8 % which is significantly lower than the use of a solid-state HTL, Spiro-OMeTAD, that reported a PCE of close to 10 % with an approximate V_{OC} of 1 V, thus showing the importance of contacts used (Kojima, Teshima, Shirai and Miyasaka, 2009; Leijtens et al., 2014). Besides that, Mora-Seró (2018) also stated that despite using the same deposition method for the perovskite layer, the nucleation and crystal growth processes of the perovskite layer will still be influenced by the contacts used.

2.2.2 Commercialization Problem of PSC

Despite the advantages of PSCs, they still face the problem of commercialization due to various reasons with the lack of long-term operational stability being one of the main factors. In contrast, silicon solar cells that have been commercialized usually can last between 25 to 30 years, proving its exceptional operational stability when compared to PSCs (Kazmerski, 2006). The key factor to commercializing a solar cell is the need for a compelling market advantage over the existing market technologies, which include low processing costs, high PCE, ease of fabrication, high stability and so on. Currently, PSCs have achieved a record PCE of 25.5 %, allowing them to exceed the efficiency of copper indium gallium selenium solar cells, and also approaching the level of crystalline silicon solar cells (Green et al., 2020). Apart from that, the major components that form the perovskite compound consist of lead and iodine, which are both abundant materials and of low cost. However, another concern for the commercialization is the toxicity of the lead element and its risk towards the environment as bad weather conditions may cause the leakage of lead elements. However, there has been ongoing research and development on producing lead-free PSCs which have been proven to reach a PCE of 11.22 %. The replacement of lead with tin is done so to reduce the defect density that is present in tin halide-based perovskite films through the template-growth deposition method (Liu et al., 2020). Besides that, the scaling up of the solar module area of PSCs is also part of the challenge towards commercialization. Figure 2.2 shows the decrease in PCE to 19.6 % as the

aperture area of PSC increases from 0.1 cm^2 to 10 cm^2 , followed by a further decrease of PCE to 17.9 % as the area approaches 1000 cm^2 .

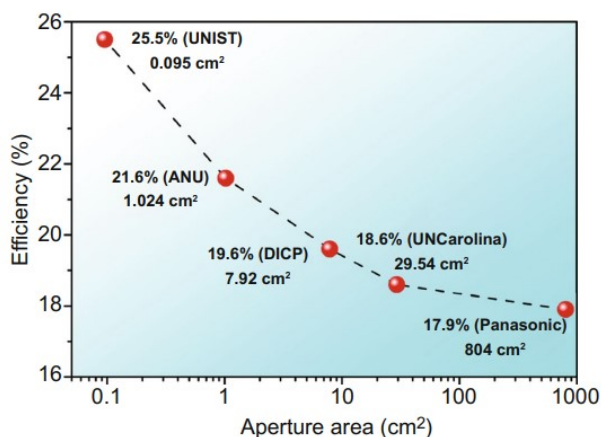


Figure 2.2: Efficiency of PSCs Against Aperture Area In 2020 (Wu et al., 2021).

As mentioned before, stability issues still pose a large obstacle towards the path of commercialization. This may be due to the fact that the components in metal halide perovskites are bonded to each other through weak bonds, which include hydrogen bond, van der Waals forces and so on. Moreover, exposure to moisture and prolonged light, stress from heat and external electric fields will induce the irreversible breakdown of organic molecules and ion migration in PSCs. These factors will result in damage towards both the perovskite and the charge transport layers, which in turn will also affect the efficiency of the PSC (Su et al., 2020; Yuan and Huang, 2016; Saidaminov et al., 2018). Nonetheless, various research and development are still ongoing to identify the factors for the various stability issues and to improve the stability of PSC for the purpose of commercialization. The efforts include using improved contact materials, substitution of ions, encapsulation of perovskite layer and so on (Snaith, 2018).

2.3 Structure of PSC

Throughout the history for the development of PSCs, the typical layer-by-layer architecture can be seen. A common structure of PSC consists of five layers which include transparent conductive oxide (TCO), ETL, perovskite layer, HTL, and the counter electrode.

Starting from the layer in which light is incident upon, TCO acts as an optically transparent electrode that absorbs light in the form of photons into the PSC (Klein et al., 2010). After that, either a HTL or ETL is deposited on top of the TCO to act as CTLs. Because of this, the PSC structure can be classified as either n-i-p or p-i-n based on the order of the functional layers in the device in which case the n-i-p is termed as the normal structure while the p-i-n architecture is termed as the inverted structure. Figure 2.3 shows the difference between the n-i-p structure and the p-i-n structure in terms of their relative locations of the CTLs.

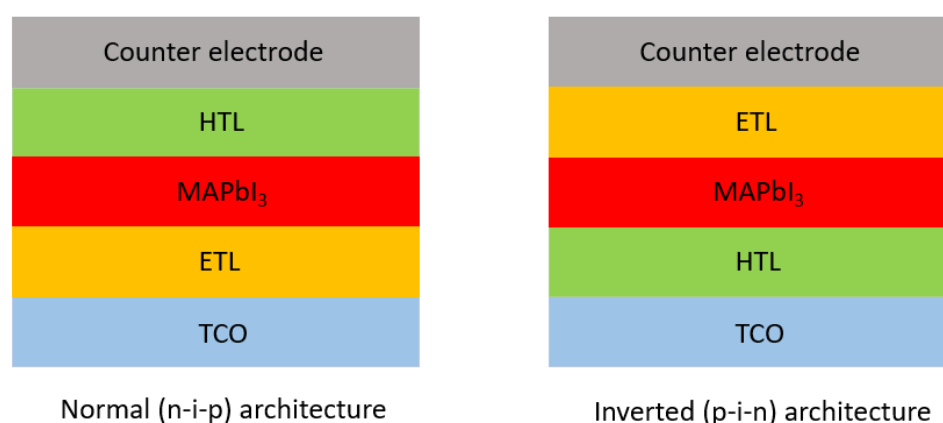


Figure 2.3: N-i-p and P-i-n Structure of PSC.

For n-i-p architecture, the ETL is deposited above the TCO while for the p-i-n architecture, the HTL is deposited on above the TCO. The perovskite layer, MAPbI₃ is sandwiched between the HTL and ETL, and lastly, the counter electrode is at the uppermost layer.

In a PSC structure, the charge carrier transfer process along various interfaces especially at the perovskite/ETL interface, and the perovskite/HTL interface is important for achieving high PCE and stability. Besides that, different materials used for ETL and HTL are also crucial in enhancing charge carrier extraction and minimizing charge recombination (Cheng et al., 2020). Moreover, the operational stability of the PSC is also deeply affected by the different types of CTLs used. Therefore, throughout the development of PSCs, different types of organic and inorganic materials have been utilized for CTLs to investigate their effects on the performance and stability of PSCs.

2.3.1 Organic CTLs

Common PSC structures usually involve the incorporation of organic CTLs since they can offer high efficiency and reduced hysteresis, nonetheless, worries about device stability still persist. Besides that, organic CTLs can be deposited above the perovskite layer without post-annealing through the use of a perovskite-compatible facile solution process (Soo et al., 2022). Since no post-annealing is required, the MAPbI₃ perovskite layer beneath would not be subjected to any heat from annealing, thus preventing thermal degradation of the perovskite layer. However, the operational stability of PSC remains as one of the major challenges for commercialization, thus the poor stability of the organic CTLs cannot be neglected.

Organic CTLs such as phenyl-C₆₁-butyric acid methyl ester (PCBM) and so on had been shown to cause stability problems when used as CTLs in PSC. For instance, the poor ion migration suppression capability of PCBM has allowed methylammonium cations (MA⁺) and iodide anions (I⁻) from MAPbI₃ film to diffuse through the PCBM and reach the silver (Ag) electrode under a thermal condition of 85 °C, leading to a drop in PCE due to the deterioration of both the counter electrode and the MAPbI₃ film (Li et al., 2017). Besides that, it was stated that the organic CTL itself such as Spiro-OMeTAD is weak against heat exposure whereby signs of degradation can be observed at an elevated temperature of 85 °C. Additionally, since ions can diffuse easily in organic molecules, the electrical properties of Spiro-OMeTAD are weakened by ion migration into it, causing a decrease in the ability of charge extraction through the formation of energy barriers (Kim et al., 2017). Apart from that, Domanski et al. (2016) also stated that gold (Au) from the counter electrode can diffuse easily through Spiro-OMeTAD and into the perovskite layer at an aging temperature of 70 °C, leading to the degradation of the PSC performance. The degradation of the performance of PSC may be due to Au creating shunts across the device while at the same time creating deep trap states that will increase charge recombination. These factors will lead to the reduction of FF, V_{OC} , and J_{SC} , which in turn leads to the overall degradation of the PSC performance.

The weak stability of organic CTLs upon heat, moisture and oxygen exposure will induce further degradation of the overall stability of PSC. You et

al. (2015) stated that the devices incorporating PCBM experience significant degradation only after 5 days when placed in an ambient environment under a temperature of 25 °C with a relative humidity of 30-50 %. This phenomenon is due to the fact that PCBM layer will undergo degradation by itself upon exposure to oxygen or water. Upon the self-degradation of PCBM, insufficient protection is provided, causing the perovskite and the counter electrode to be directly in contact with each other, thus damaging both of them. Apart from that, according to the research done by Jena et al. (2018), it was shown that the performance degradation of the MAPbI₃ solar cells occur as a result of generation of voids in Spiro-OMeTAD and chemical modification at the perovskite/Spiro-OMeTAD interface at an elevated temperature of 60, 80, 100 and 120 °C. The deformation of Spiro-OMeTAD as a result of weak thermal stability has caused further degradation of the perovskite layer, which in turn affects the overall PSC performance.

2.3.2 Inorganic CTLs

In contrast to the organic CTLs, inorganic CTLs exhibited a significant improvement in stability. The improved chemical stability, together with the ability of inorganic CTLs to act as a good barrier against oxygen and moisture ingress, followed by good ion migration suppression, is what gives the enhanced stability (Soo et al., 2021; Guo et al., 2020). The most commonly used inorganic CTLs would be metal oxides.

Shin, Lee and Seok (2019) stated that metal oxides are able to exhibit good electrical properties, together with good resistance towards moisture, heat, and light. In their study, it was found that when nickel oxide (NiO_x) was used as the HTL, the performance of the PSC was able to preserve more than 80 % of its initial effectiveness after being stored in a glove box filled with nitrogen for 40 days. On the other hand, PSC utilizing PCBM as the HTL has shown a sharp degradation of the performance in the same condition. Apart from that, it was stated that the utilization of NiO_x and zinc oxide (ZnO) as the HTL and ETL respectively has shown that the retention in performance of the device for 60 days after storage in an atmosphere with 25 °C and 30–50 % humidity, however, the performance of the organic charge transport layer-based device

was drastically lost after just 5 days. Moreover, the NiO_x-based PSCs can withstand solar illumination at 85 °C for more than 1000 hours whereas the organic transport layer-based PSC can only last for 5 days without performance degradation. Furthermore, Chen et al. (2015) also proved the improved stability of PSC with the utilization of metal oxide as CTL, whereby it was stated that PSC incorporating titanium-niobium oxides (Ti(Nb)O_x) as CTL showed a PCE degradation of only less than 10 % when exposed to full sunlight of a solar simulator for 1000 hours.

It has been reported that metal oxides can be directly deposited above the perovskite layer without the need for after-treatment such as annealing thanks to atomic layer deposition (ALD) and physical vapour deposition (PVD) techniques like thermal evaporation and so on (Guo et al., 2020; Lei et al., 2019). However, the deposition of the metal oxide CTLs using these techniques requires specialized and expensive equipment. Furthermore, the inability of these deposition techniques to be scalable is also another detrimental effect towards the commercialization of PSCs (Soo et al., 2021). Apart from magnetron sputtering and thermal evaporation, the metal oxide nanoparticle (NP) route has also been shown to successfully deposit metal oxide CTLs on the perovskite layer (You et al., 2015; Liu et al., 2018). Some of the benefits of this deposition method include the low cost of the NPs, and the ability of NPs to be produced in significant quantities under ambient air, followed by the requirement of less sophisticated and low-cost technology such as spin coating and facile solution process (Icli and Ozenbas, 2018; Soo et al., 2022). However, metal oxide NPs still face the problem of agglomeration which is due to the adhesion of particles to one another by weak forces. Thus, the countermeasure for this problem is to add ligands to the NPs for stabilization effect (Gosens et al., 2010; Ouyang, Huang and Choy, 2018). Nonetheless, the stabilizing ligands have to be removed as they may inhibit charge transfer between particles. Besides that, it was also reported by Liu et al. (2017) that hysteresis may occur as a result of leftover ligands on the NiO particles. Thus, it is clear that ligands must be removed after deposition and removed before deposition using ligand-exchange method as mentioned by Papadas et al. (2019) to prevent any inhibition of charge transfer between the NPs. Furthermore, Icli and Ozenbas (2018) also mentioned that the thickness of the metal oxide NPs CTL needs to

be optimized to minimize charge transfer resistance and provide full coverage of the perovskite layer, whereby the thickness should be lower than 200 nm but higher than 50 nm. As a result, it is clear that the metal oxide NP route has a lot of complexities in terms of its deposition process and thus will not be utilized.

A better alternative for the metal oxide NP route would be the utilization of metal oxide sols. Compared to metal oxide NPs, metal oxide sols have a number of advantages. First of all, Zhang, Tang, Wu and Lan (2019) stated that metal oxide sols provide better substrate coverage uniformity. For instance, NiO HTLs fabricated through facile nickel-containing organic sol route can provide higher surface coverage when compared to NiO nanocrystals solution. Furthermore, in the absence of ligand stabilization, metal oxide sols can resist agglomeration for a lengthy period. Besides that, by dissolving their precursors in the solvents, metal oxide sols can be made quickly and then applied to a substrate using a facile solution process. Unfortunately, metal oxide sols require high annealing temperature after deposition to form compact CTLs, while at the same time attaining high crystallinity for effective charge transportation (Soo et al., 2021; Soo et al., 2022). For instance, the conventional titanium dioxide (TiO_2) metal oxide sol is annealed at a high temperature of 500 °C after deposition (Qin et al., 2017). Since a high annealing temperature is required for these metal oxide sols, the deposition of these metal oxide sols above MAPbI_3 films seems unlikely since MAPbI_3 films have low thermal stability. This is why these high-temperature processed metal oxide sols are only utilized when deposited below the perovskite layer. However, metal oxide sols with low annealing temperature have recently been on the trend due to their competitive advantage when compared with metal oxide sols that require high processing temperature. The reason being that the low annealing temperature not only can save production cost but also decrease the risk of thermal degradation of the perovskite layer when deposited above it. Examples of metal oxide sols with low annealing temperatures of less than or equal to 150 °C include TiO_2 , zinc oxide (ZnO), tin (IV) oxide (SnO_2) and so on (Chan, Chang and Wu, 2019). It was also stated that these low-temperature processed metal oxide sols can still maintain high efficiency of PSC due to their high conductivity, and passivation at the perovskite/CTL interface. Therefore, to develop an ideal PSC with metal oxides as its CTLs, improvement on thermal

stability of the MAPbI₃ film should be made to withstand any potential thermal degradation that would affect the performance of the PSC.

2.4 Stability of MAPbI₃ Layer

In order to counteract the thermal effect from the annealing of metal oxide sols, the MAPbI₃ layer needs to be enhanced in terms of its thermal stability. Nonetheless, apart from thermal stability issues, the MAPbI₃ layer also suffers from other stability issues such as moisture and oxygen.

2.4.1 Moisture Stability

Cao et al. (2015) stated that the MA⁺ cations of MAPbI₃ are highly hygroscopic, meaning that it tends to absorb moisture from the air, thus allowing moisture to easily break down the structure of MAPbI₃. This is because the ammonium from the perovskite layer is easily removed from the perovskite structure by water, a Lewis base, and thus allows the perovskite structure to break down easily. To counteract, it was stated that MAPbI₃ films treated with both the carboxylic acid and thiol groups (HOOC-Ph-SH) and hydrophobic thiols (HS-PhF₅) developed a better performance in terms of stability when compared to the MAPbI₃ film without any treatment of HS-PhF₅. Figure 2.4 shows the colour variation of HOOC-Ph-SH/perovskite/Spiro-OMeTAD and HOOC-Ph-SH/perovskite/HS-PhF₅/Spiro-OMeTAD films when stored in air with 45 % humidity at room temperature for 8 days.

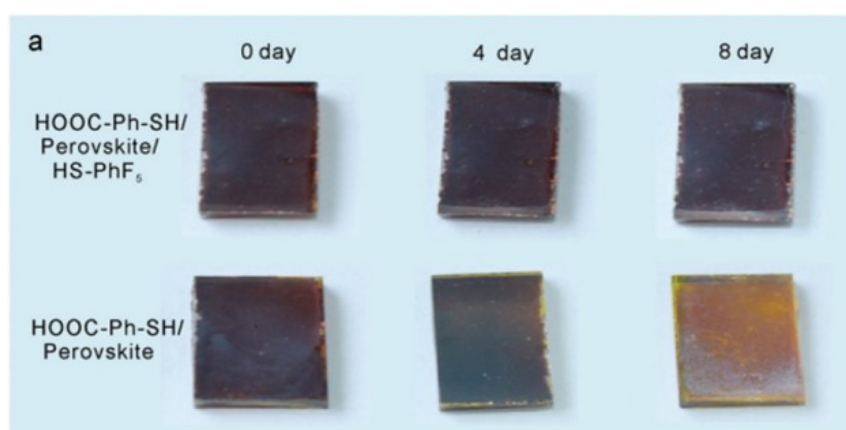


Figure 2.4: Colour Variation of HOOC-Ph-SH/Perovskite/Spiro-OMeTAD and HOOC-Ph-SH/Perovskite/HS-PhF₅/Spiro-OMeTAD Films (Cao et al., 2015).

The results have shown that the PSC without any treatment from hydrophobic thiol groups suffered degradation, as seen by the decaying of a dark colour to yellow on day 8. Thus, this signifies that the MAPbI₃ layer is also subjected to the risk of stability due to moisture ingress. Besides that, Habisreutinger et al. (2014) also stated that the introduction of water molecules into the perovskite crystal structure will lead to the formation of weak hydrogen bonds with the MA⁺ cations, resulting in the dissociation of bonds between the crystal constituents. Thus, the yellow colour of the degraded PSC is due to the escaping of the MA⁺ and I⁻ ions, leaving behind the yellow colour lead (II) iodide (PbI₂).

2.4.2 Oxygen Stability

Other than degradation suffered from moisture, there is also a potential risk of oxygen degradation in PSC. It is demonstrated by Pearson et al. (2016) that PSC will deteriorate to 20 % of its initial performance after several hours of exposure to Air Mass (AM) 1.5 G of simulated sunlight in 10 % of dry oxygen (O₂). Besides that, Aristidou et al. (2015) stated that the mechanism behind oxygen degradation involves the formation of superoxide anions (O₂⁻) as the oxygen molecule comes into contact with excited photoelectrons from the perovskite conduction band. The resulting action would be O₂⁻ deprotonating the MA⁺, which would result in the decomposition of MAPbI₃ to lead iodide and methylamine.

2.4.3 Thermal Stability

Finally, the main stability issue would be the weak thermal stability of the MAPbI₃ film as the whole purpose is to enable the annealing of metal oxide sol above the MAPbI₃ film without thermal degradation. Conings et al. (2015) stated that the MAPbI₃ layer showed initial signs of degradation when it is thermally annealed at 85 °C in a pure dry nitrogen atmosphere (N₂). Figure 2.5 shows the SEM results of the MAPbI₃ film after the annealing process.

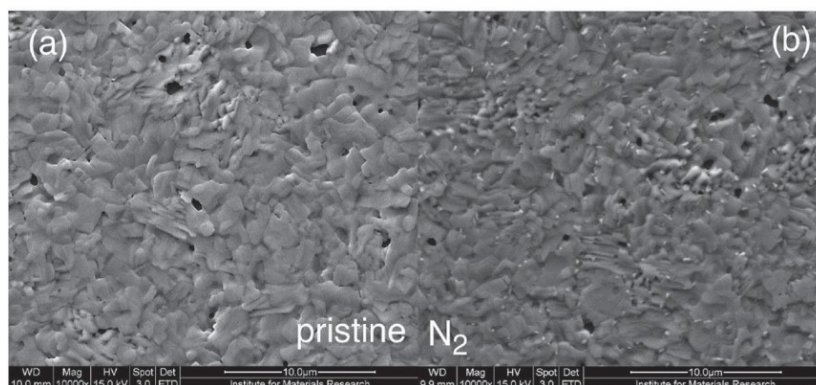


Figure 2.5: SEM Images of ITO/TiO₂/Perovskite Samples in Pristine and N₂ Atmospheres at 85 °C For 24 Hours (Conings et al., 2015).

The results of the SEM images have clearly shown differences in the morphology that can be seen through the formation of speckles and tiny needles which are proven to be PbI₂ grains, thus proving the initial degradation of the perovskite layer due to thermal effect. Apart from that, MAPbI₃ was also shown to have weaker thermal stability than formamidinium lead iodide (FAPbI₃) when heated at a high temperature of 150 °C (Eperon et al., 2014; Yang et al., 2017). Figure 2.6 shows the comparison in colour between MAPbI₃ and FAPbI₃ when heated at 150 °C, whereby the obvious colour change of MAPbI₃ from dark brown to yellow signifies thermal degradation to PbI₂ when compared to the constant colour appearance of FAPbI₃ even after 60 minutes of heating.

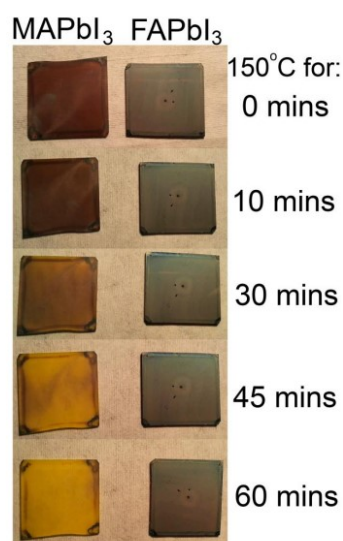


Figure 2.6: Thermal Degradation Comparison of MAPbI₃ and FAPbI₃ When Heated at 150 °C (Eperon et al., 2014).

Furthermore, Chaudhary et al. (2020) also reported the rapid thermal degradation of MAPbI₃ films at 150 °C whereby signs of yellow variation in colour can be observed after 60 minutes of heating and ultimately full degradation took place after 90 minutes. Ultimately, all these findings pointed out the fact that MAPbI₃ films will thermally degrade at 150 °C which is the annealing temperature for most low-temperature processed metal oxide sols. Therefore, it is crucial to find solutions towards the enhancement of thermal stability for MAPbI₃ film so that metal oxide sols can be deposited above it.

2.4.4 Thermal Stability Enhancement of MAPbI₃ Film by PMMA Encapsulation

One of the methods to increase the thermal stability of MAPbI₃ is to perform PMMA encapsulation on the perovskite layer.

Soo et al. (2021) reported that under the annealing temperature of 150 °C, PMMA-encapsulated MAPbI₃ films can last for a longer period of time before it starts to show obvious signs of thermal degradation at 180 minutes. This result is significantly better than the previously reported results by Chaudhary et al. (2020) and Eperon et al. (2014) whereby the unencapsulated MAPbI₃ films can only last up to 60 minutes before it starts to thermally degrade. Figure 2.7 shows the XRD results for the annealed MAPbI₃ films at 150 °C for various durations.

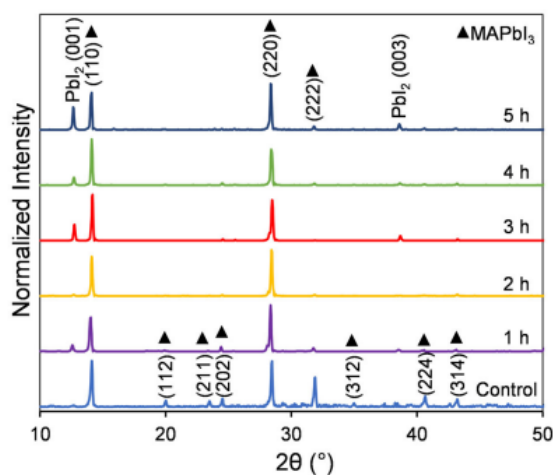


Figure 2.7: XRD Results of Control and PMMA-Encapsulated MAPbI₃ Films at 150 °C at Different Periods (Soo et al., 2021).

The results from the XRD patterns have shown that the appearance of PbI_2 peaks at the (001) and (003) planes start to become more observable when the annealing time reaches 3 hours onwards. Besides that, the diminishing of the minority MAPbI_3 peaks for 3 hours and onward of annealing time also signified the commencement of thermal degradation at 3 hours of annealing. Moreover, based on the colour distinction of the MAPbI_3 films as shown in Figure 2.8, the PMMA-encapsulated region was able to retain the dark brown colour of the film for 180 minutes before it starts to show signs of bleaching, indicating the start of thermal degradation.

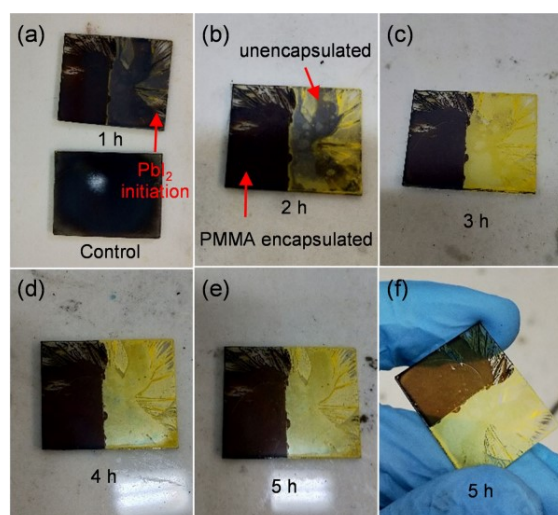


Figure 2.8: Physical Appearances of Annealed MAPbI_3 Films with Both PMMA-Encapsulated and Unencapsulated Portion at Various Durations (Soo et al., 2021).

This result is in contrast with the previous results reported by Eperon et al. (2014) and Chaudhary et al. (2020) whereby the colour of their MAPbI_3 films showed signs of yellow variation only after 30 minutes of annealing.

It was reported that the encapsulation of PMMA served as a passivation mechanism towards the defect sites at the grain boundaries (GB) of the MAPbI_3 polycrystalline film at the interface between the film and air whereby the defects comprise of halide vacancies and Pb-halide antisites (Soo et al., 2021). Besides that, these defects were reported to be the cause for the increment of ion migration as they tend to reduce the activation energy needed for ion migration.

Once the activation energy required for migrating ions is reduced, the ions will require less energy to migrate to other places, which in turn leads to the release of volatile MAI from GBs (Shao et al., 2016; Lee et al., 2019). As mentioned previously, thermal degradation causes the dark brown colour of the MAPbI₃ film to turn yellow, indicating the reduction of MAPbI₃ to PbI₂ as caused by the escape of volatile MAI from GBs. This occurrence may be due to the halide ions gaining sufficient energy from thermal annealing, which in turn allows them to move to the defect sites at the GBs which serve as channels for the escape of volatile MAI (Soo et al., 2022). Therefore, it is crucial to target the passivation mechanism at the GBs first as an effort to minimize ion migration while at the same time enhancing both the thermal and operational stability (Li et al., 2018; Soo et al., 2021). Furthermore, Zhao et al. (2021) stated that it is generally accepted that charge accumulation between interfaces is what causes perovskite hysteresis. Since this charge accumulation is primarily brought on by ion migration, the more the reason for the suppression of ion migration at the GBs.

Lan, Wang and Song (2020) have reported the use of polycaprolactone (PCL), a kind of polymer additive, in passivating the defects at the GBs due to the interaction between the carbonyl group (C=O) and Pb²⁺ of the MAPbI₃ film. The result was the increment in the PCE from 10.52 % to 14.49 % due to lower defect-induced recombination at the GBs. Besides that, polymers with carbonyl groups such as PMMA and poly(propylene carbonate) (PPC) are reported to act as Lewis base site whereby the lone pair electrons of the Lewis bases' could interact with the under-coordinated Pb atoms at the GBs to form a dipole-ion interaction, which is thought to be the mechanism through which the Lewis bases and perovskite interact (Han et al., 2019; Peng et al., 2018). Furthermore, Soo et al. (2021) added that the lone pair of electrons in the carbonyl group of PMMA established a coordinative bond with the I vacancy at GBs at the MAPbI₃ film/air interface as shown in Figure 2.9.

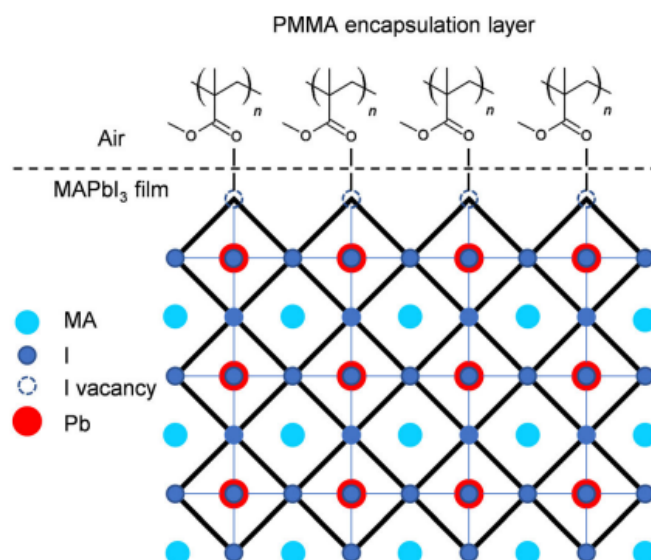


Figure 2.9: Passivation Mechanism on GBs by Carbonyl Group of PMMA (Soo et al., 2021).

The passivation mechanism as shown in Figure 2.9 increases the activation energy for ion migration and is reported to be the reason for the suppression of the volatile MAI from escaping at the GB defects located at the interface between the MAPbI₃ film and air, which in turn reduced the thermal degradation of the MAPbI₃ film at 150 °C.

2.4.5 Thermal Stability Enhancement of MAPbI₃ Film Through Incorporation of PMMA Additives

In general, additive engineering is a practical methodology to produce perovskite films that have better quality and lower number of defects. By incorporating polymer additives into perovskite films, the defects at the GBs can be passivated through bonding interactions (Doosthosseini et al., 2020).

For instance, it was reported that the thermal stability enhancement of MAPbI₃ film using the formation of a continuous network polymer through in-situ cross-linking of the carbonyl groups of trimethylolpropane triacrylate (TMTA) with the GBs of MAPbI₃ film (Li et al., 2018). The result has shown a significant increase in thermal stability, whereby the cross-linked device retained over 80 % of PCE when subjected to heating at 85 °C in a N₂-filled glovebox. In contrast, the devices without any TMTA passivation only retained 45 % of their initial PCE. This occurrence may be possible due to the interaction

between the carbonyl groups of TMTA with the PbI_2 , thus allowing TMTA to anchor to the GBs at MAPbI_3 film and passivate its defects.

Apart from polymer additives, other additives that are not volatile such as caffeine have also proven to increase the thermal stability of the MAPbI_3 film. Figure 2.10 shows the comparison of XRD patterns between PMMA-encapsulated MAPbI_3 films with and without the addition of caffeine when annealed at $150\text{ }^\circ\text{C}$ for various hours.

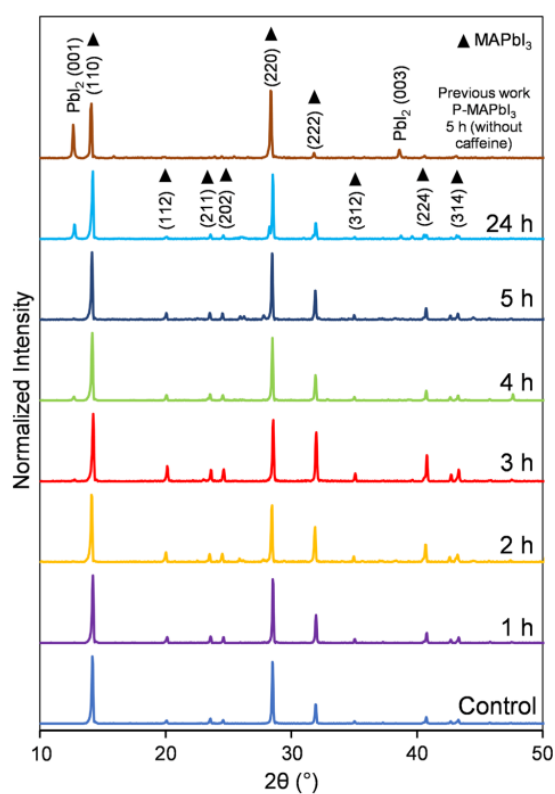


Figure 2.10: XRD Patterns Between PMMA-Encapsulated MAPbI_3 Films with and Without the Addition of Caffeine When Annealed At $150\text{ }^\circ\text{C}$ for Various Hours (Soo et al., 2022).

Based on Figure 2.10, the ratio of the peak intensity of PbI_2 at (001) plane to MAPbI_3 at (110) plane is 0.61 for the PMMA-encapsulated MAPbI_3 film without the addition of caffeine (5 hours), while it is only 0.27 for the PMMA-encapsulated MAPbI_3 film with the addition of caffeine (24 hours). This lower PbI_2 peak ratio of 0.27 has proven that the addition of caffeine has enhanced the thermal stability by a significant amount, especially when considering the huge

difference in the number of hours annealed at the temperature of 150 °C. It was reported that the passivation mechanism behind the addition of caffeine attributed to the function of the carbonyl group of caffeine molecule to interact with the under-coordinated Pb^{2+} defect sites located at the GBs within the MAPbI_3 film as shown in Figure 2.11 (Wang et al., 2019; Soo et al., 2022).

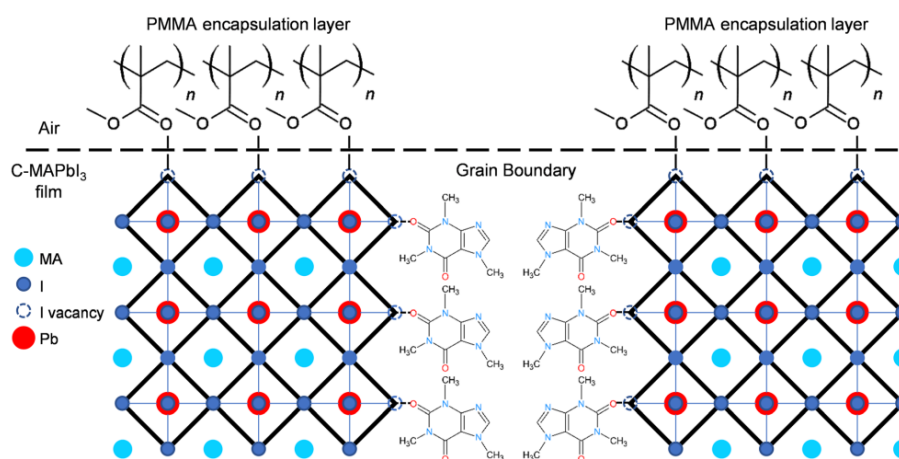


Figure 2.11: Passivation Mechanism of Caffeine at GBs Within MAPbI_3 Film (Soo et al., 2022).

Like caffeine and TMTA as reported previously, PMMA possesses a carbonyl group that has been shown to passivate the defects at the GBs of the MAPbI_3 film. Besides that, Bi et al. (2016) have reported the use of PMMA in polymer-templated nucleation and growth (PTNG), whereby the addition of PMMA helped to trigger heterogeneous nucleation over the perovskite film. At the same time, PMMA was also able to form an intermediate adduct with PbI_2 , delaying the growth of perovskite crystals which in turn allowed the randomly generated nuclei to modify their orientation and grew in the thermodynamically favourable orientation. The formation of the intermediate adducts between PMMA and PbI_2 was proven by the result of Fourier Transform Infrared Spectroscopy (FTIR) whereby the shifting of the stretching $\text{C}=\text{O}$ vibration in PMMA from 1735 cm^{-1} to 1723 cm^{-1} indicated the interaction between the carbonyl group of PMMA (Lewis base) and PbI_2 (Lewis acid) as a result of weakened $\text{C}=\text{O}$ bond strength as shown in Figure 2.12.

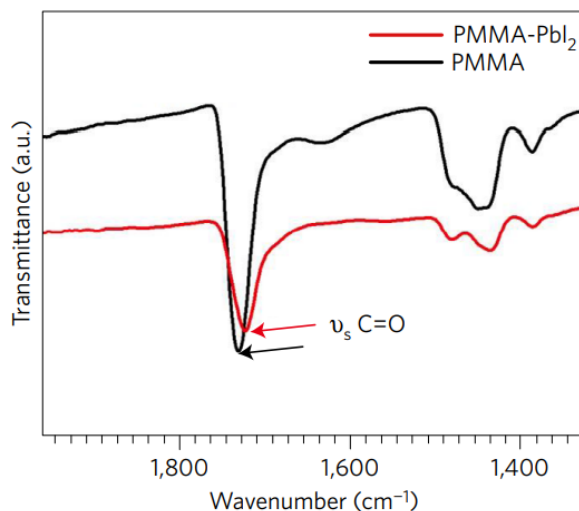


Figure 2.12: FTIR Spectra of PMMA-PbI₂ Mixture and Pristine PMMA Films (Bi et al., 2016).

Furthermore, Figure 2.13 shows the cross-sectional SEM results of perovskite films deposited by PTNG method after annealing at 100 °C with different concentrations of PMMA added.

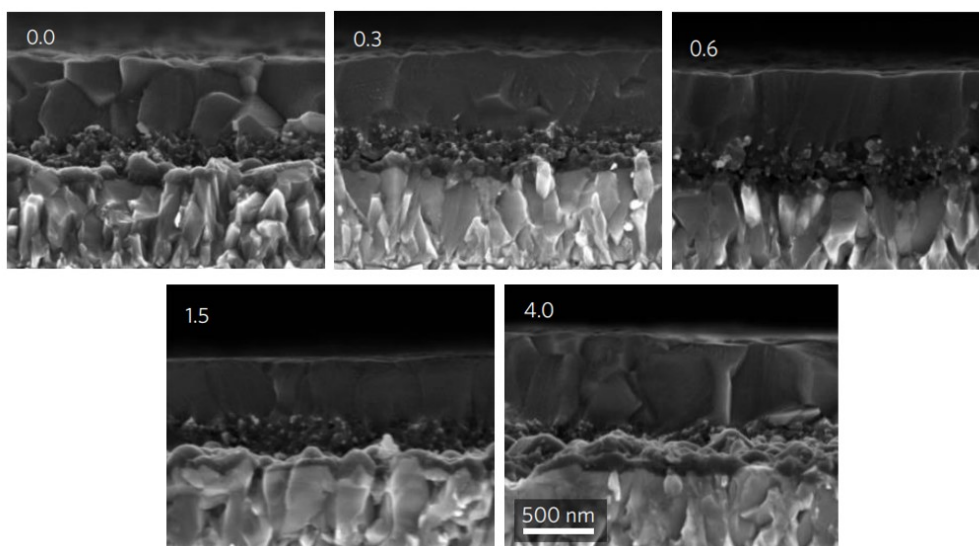


Figure 2.13: Cross-Sectional SEM Results of Perovskite Films with Various Concentrations of PMMA Added (Bi et al., 2016).

From Figure 2.13, it can be seen that the higher the concentrations of the PMMA added, the larger the grain size of the perovskite film and the lower the surface area of the GBs as a result of the GBs becoming more perpendicular to the

substrate. These results increased the potential of PMMA additives contributing to the enhancement of thermal stability of the MAPbI₃ films. Moreover, it was reported by Park et al. (2017) that MAPbI₃ perovskite crystals have higher thermal stability with larger grain sizes as shown in Figure 2.14, whereby the increase in PCE was accompanied by the increase in grain size of the MAPbI₃ perovskite crystals after annealed at 100 °C for 30 minutes. This hypothesis implies that a larger grain size will reduce the number of defect sites at GBs as a result of the smaller surface area of GBs, thus impeding ion migration and enhancing the thermal stability of MAPbI₃ film.

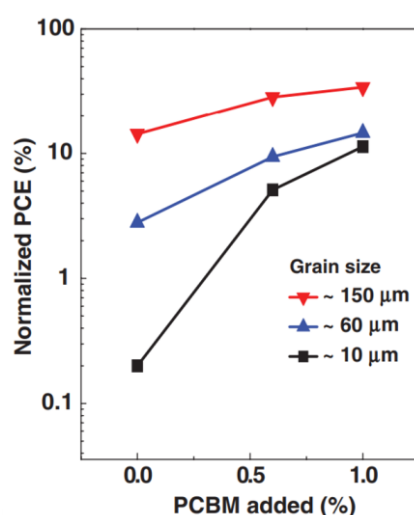


Figure 2.14: Normalized PCEs with the Initial PCE After Annealing at 100 °C As a Function of PCBM Added (Park et al., 2017).

Apart from that, as previously reported by Soo et al. (2022) and Soo et al. (2021), PMMA should be able to perform the same passivation mechanism at the GBs within the MAPbI₃ film. As shown previously in both Figure 2.9 and Figure 2.11, the carbonyl functional groups are an important part of the passivation mechanism whereby they will form coordinative bonds with the iodide vacancies at the defect site of the GBs. Passivation at the defect site of GBs is reported to be essential towards the enhancement of thermal stability as these locations are where the perovskite layer starts to degrade due to the greater spacing brought on by junctions of inconsistent lattices and structural defects (Castro-Méndez, Hidalgo and Correa-Baena, 2019).

2.5 Summary

To improve the overall stability of MAPbI₃ film, organic CTLs were found to be less effective when compared to inorganic CTLs such as metal oxides. The deposition of metal oxide sols on MAPbI₃ films is found to be beneficial in many ways for the development of PSC towards enhanced stability. Nonetheless, it was found that the weak thermal stability of MAPbI₃ film posed a problem for direct annealing of metal oxide sols above it. To counteract this problem, various methods have been studied with hopes of improving the thermal stability of MAPbI₃ films, which include encapsulation using PMMA, and incorporation of additives with low volatility such as caffeine and so on. The incorporation of PMMA additives and dual PMMA encapsulation layers will be further studied in this work for its potential for further thermal stability enhancement of the MAPbI₃ film.

CHAPTER 3

METHODOLOGY AND WORK PLAN

3.1 Introduction

In this study, the first part of the experiment involved the incorporation of PMMA as an additive to the MAPbI₃ film through two ways, whereby the first method involved the use of vacuum-assisted solution processing (VASP) while the second method involved the use of antisolvent-assisted one-step spin-coating, resulting in the formation of PMMA-MAPbI₃ film. The preparation of the PMMA-MAPbI₃ film involved different amounts of PMMA additives to investigate the effect of the increment of additives added on the thermal stability enhancement. The structure of the samples produced using VASP and antisolvent method are shown in Figure 3.1 (a). Besides the addition of additives, PMMA encapsulation was also performed by spin-coating it on top of the PMMA-MAPbI₃ film. For the second part of the experiment, to investigate the effect of dual PMMA encapsulation layers on the thermal stability of MAPbI₃ films, an additional layer of PMMA encapsulation was added beneath the perovskite layer of pristine MAPbI₃ films. The sample structure of dual PMMA-encapsulated sample is shown in Figure 3.1 (b). After the preparation of samples, SEM, XRD and UV-Vis spectroscopy analyses were performed to study the morphologies and absorbance spectra of the films.

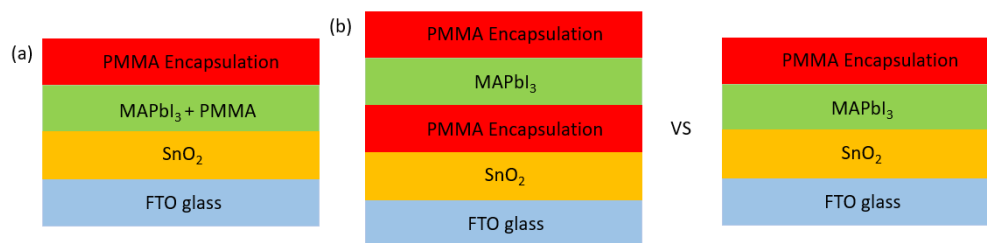


Figure 3.1: Sample Structures: (a) VASP and Antisolvent Method, (b) Single and Dual PMMA Encapsulation.

3.2 Spin-coating of SnO₂ Solution on the Fluorine-Doped Tin Oxide (FTO) Glass Pieces

Before depositing the SnO₂ solution onto films, FTO glass slides must first be prepared. Firstly, multiple substrates were created from the FTO glass slides by cutting them into pieces of 2 cm × 1.5 cm. After that, to ensure that the glass slides were free from unwanted particles, an ultrasonic cleaner was used to clean the substrates with acetone first, followed by isopropanol, and distilled water for 10 minutes each.

Then, to increase the affinity of the glass substrates towards the deposition of SnO₂ solution, they were placed on a hot plate to be heated at 480 °C for 45 minutes. The heating process also helped to remove any organic residues that are left unattended. After the heating process, the glass substrates underwent UV ozone process for 20 minutes before any solution is spin-coated onto it. The stock SnO₂ colloidal solution (non-toxic solution) was mixed with distilled water with a weight ratio of 1:3 before being stored in a 50 mL HDPE bottle. By utilizing a spin-coater, 100 μL of SnO₂ colloidal solution was spin-coated onto the FTO glass slide that was placed on the spin-coater chunk at 4000 rpm for 30 seconds as shown in Figure 3.2. Then, the SnO₂ coated FTO glass was heated on a hot plate at 150 °C for 45 minutes.

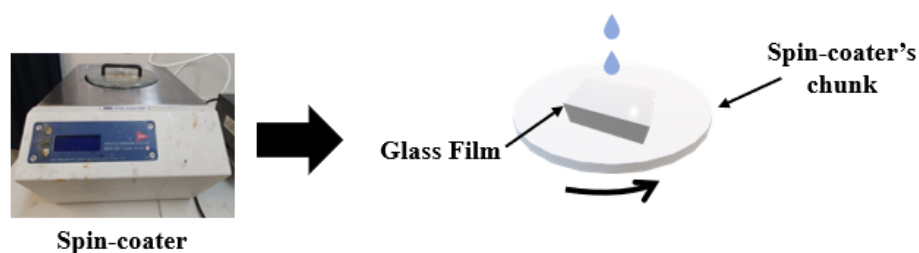


Figure 3.2: Illustration for Spin-coating of SnO₂ onto FTO Glass.

3.3 Methodology for MAPbI₃ Films with Incorporation of PMMA Additives Using VASP

The first part of the experiment involved using VASP to produce PMMA-MAPbI₃ films.

3.3.1 Preparation of MAPbI₃ Precursor Solution with the Addition of PMMA

The precursor solution for MAPbI₃ with the incorporation of PMMA additives (PMMA-MAPbI₃) was prepared by utilizing PMMA, MAI, PbI₂, dimethyl sulfoxide (DMSO) and dimethylformamide (DMF). To produce the precursor solution, 1 mg of PMMA, 461 mg of PbI₂ and 159 mg of MAI were put inside a glovebox to be weighed using an analytical balance. To reduce the interactivity with oxygen and moisture in the surrounding air, they were immediately dissolved in 100 μ L DMSO and 900 μ L DMF (1:9 ratio) after being transferred out of the glovebox as shown in Figure 3.3. After that, to prevent further interaction with light, stirring was performed on the precursor solution in the dark for 1 hour. Then, to ensure that the precursor solution is free from any solid impurities, a 0.2 μ m polytetrafluoroethylene (PTFE) syringe was used to filter the solution. To investigate the thermal stability enhancement effect by the amount of PMMA additive added, the same experimental steps were used to create other PMMA-MAPbI₃ precursor solutions with different amounts of PMMA added for each set of data, namely, 0, 3, 5 and 7 mg. The purpose of the data set with 0 mg of PMMA is to act as a control film to study the thermal stability enhancing capability of PMMA additives.

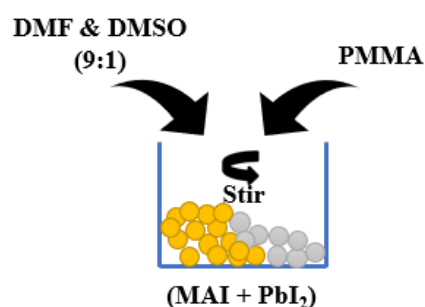


Figure 3.3: Illustration for Preparation of MAPbI₃ Precursor Solution with the Addition of PMMA Additives.

3.3.2 Preparation of PMMA Solution

To obtain PMMA solution for the purpose of PMMA encapsulation, commercial acrylic sheets were utilized. Firstly, a vertical saw machine was utilized to cut the acrylic sheets into pieces, which after the pieces underwent a

cleaning process through the utilization of ultrasonication. The cleaning process was done so by utilizing dish detergent solution and filtered water whereby each process takes 10 minutes each. After that, a hot plate was utilized to fully dry the pieces at 150 °C for 2 minutes. Then, to produce a PMMA solution with a concentration of 10 mg/ mL, the acrylic pieces were dissolved in ethyl acetate in a closed container at 60 °C, followed by vigorous stirring to ensure complete dissolution as shown in Figure 3.4. 10 mg/ mL concentration was used to ensure better coverage of PMMA film on the perovskite layer (Soo et al., 2022). After that, the same steps in Section 3.2 were performed.

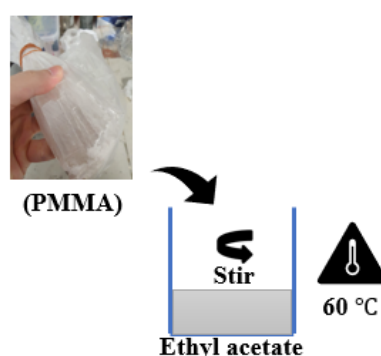


Figure 3.4: Illustration for the Preparation of PMMA Solution.

3.3.3 Deposition of PMMA-MAPbI₃ and PMMA Encapsulation Layer

By utilizing a spin-coater, in the centre of the cooled substrate, 60 μ L of the PMMA-MAPbI₃ precursor solution containing 1 mg of PMMA additives, was then spin-coated at 4000 rpm for 10 seconds. Then, the spin-coated film is immediately place in the vacuum chamber for VASP for 10 seconds to induce more uniform and homogeneous film as shown in Figure 3.5. After that, further annealing is performed on the film using a hot plate for 5 minutes at 100 °C, which resulted in the formation of a dark brown transparent film.

To form the PMMA encapsulation layer, 100 μ L of PMMA solution was deposited above the PMMA-MAPbI₃ film through spin-coating at 4000 rpm for 30 seconds by using a pipette tip. This is due to the high viscosity of the PMMA solution in which a pipette tip was used to ensure the even spreading of the solution on the PMMA-MAPbI₃ film. Then, the PMMA-encapsulated PMMA-MAPbI₃ film was heated at 100 °C for 5 minutes. These experimental

steps were repeated to create films with different PMMA-MAPbI₃ precursor solutions containing 0, 3, 5 and 7 mg of PMMA additives, respectively. After that, these films would act as control films as no annealing were performed on them. However, additional sets of these films were created with the same experimental steps and annealed at 150 °C for 1, 2, 3 and 5 hours to test the thermal stability of the films containing different amounts of PMMA additives respectively.

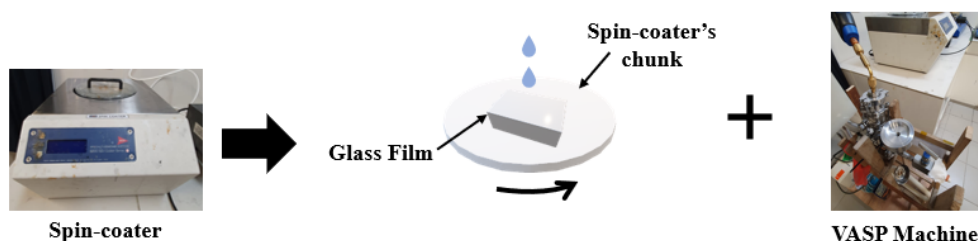


Figure 3.5: Illustration for Deposition of PMMA-MAPbI₃ Using VASP.

3.3.4 Characterizations

For physical appearance assessment, pictures of the samples were taken for every 0, 1, 2, 3 and 5 hours of thermal stressing. Without removing the PMMA layer, an XRD (Shidmazu XRD-6000, Cu K α radiation) investigation was performed to ascertain the phases present in the film. As the main method to determine the thermal stability of the MAPbI₃ films, the phase changes were studied by taking note of the values of the main MAPbI₃ and PbI₂ peaks at the diffraction angles of 14.1° and 12.6°, respectively. This is performed so that the peak intensity ratio of PbI₂ to MAPbI₃ for the samples can be tabulated by dividing the integrated intensity counts of PbI₂ with the integrated intensity counts of MAPbI₃ to compare the rate of thermal degradation.

3.4 Methodology for MAPbI₃ Films with Incorporation of PMMA Additives Using Antisolvent Method

A different method was used to produce the PMMA-MAPbI₃ films in which an antisolvent, namely ethyl acetate in this case, was utilized.

3.4.1 Preparation of MAPbI₃ Precursor Solution with the Addition of PMMA

The precursor solution for MAPbI₃ with the incorporation of PMMA additives (PMMA-MAPbI₃) was prepared by utilizing PMMA, MAI, PbI₂, DMSO and DMF. To produce the precursor solution, 461 mg of PbI₂ and 159 mg of MAI were put inside a glovebox to be weighed using an analytical balance. To reduce the interactivity with oxygen and moisture in the surrounding air, they were immediately dissolved in 71 μ L DMSO and 600 μ L DMF after being transferred out of the glovebox. After that, to prevent further interaction with light, stirring was performed on the precursor solution in the dark for 1 hour. Then, to ensure that the precursor solution is free from any solid impurities, a 0.2 μ m PTFE syringe was used to filter the solution. For the incorporation of PMMA additives, 0.05 wt % of PMMA solution was prepared beforehand by dissolving PMMA in ethyl acetate. To investigate the thermal stability enhancement effect by the amount of PMMA additive added, the same experimental steps were used to create other PMMA-MAPbI₃ precursor solutions with different amounts of PMMA added for each set of data, namely, 0, 0.10 and 0.15 wt%. The purpose of the data set with 0 wt% of PMMA additives is to act as a control film to study the thermal stability enhancing capability of PMMA additives. After that, the same steps in Section 3.2 were performed.

3.4.2 Deposition of PMMA-MAPbI₃ and PMMA Encapsulation Layer

In the centre of the cooled substrate, 45 μ L of the MAPbI₃ precursor solution containing 0.05 wt% was then drip-deposited and given 10 seconds to completely wet the substrate. A light brown transparent film was created by spinning 300 μ L of ethyl acetate antisolvent (with 0.05 wt% of PMMA dissolved in it) onto the spinning film at 10 seconds after the spin-coating was started at 4000 rpm for 30 seconds as shown in Figure 3.6. Then, further annealing is performed on the film using a hotplate for 5 minutes at 100 $^{\circ}$ C, which resulted in the darkening of the film.

To form the PMMA encapsulation layer, 100 μ L of PMMA solution was deposited above the PMMA-MAPbI₃ film through spin-coating at 4000 rpm for 30 seconds by using a pipette tip. Then, the PMMA-encapsulated PMMA-

MAPbI₃ film was heated at 100 °C for 5 minutes. These experimental steps were repeated to create films with different PMMA-MAPbI₃ precursor solutions containing 0, 0.10 and 0.15 wt% of PMMA additives, respectively. After that, these films would act as control films as no annealing were performed on them. However, additional sets of these films were created with the same experimental steps and annealed at 150 °C for 1, 2, 3 and 5 hours to test the thermal stability of the films containing different amounts of PMMA additives respectively.

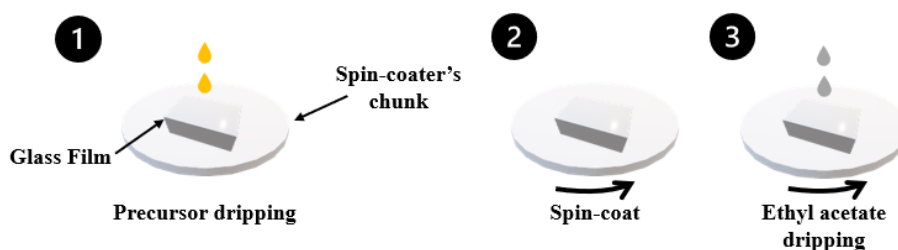


Figure 3.6: Illustration for Deposition of PMMA-MAPbI₃ Using Antisolvent.

3.4.3 Characterizations

For physical appearance assessment, pictures of the samples were taken for every 0, 1, 2, 3 and 5 hours of thermal stressing. Without removing the PMMA layer, an X-ray diffraction investigation was performed to ascertain the phases present in the film. Then, to obtain the peak intensity ratio of PbI₂ to MAPbI₃, the integrated intensity counts of PbI₂ at 12.6° were divided by the integrated intensity counts of MAPbI₃ at 14.1°.

3.5 Methodology for MAPbI₃ Films with Dual PMMA Encapsulation Layers

The second part of the experiment involved the production of MAPbI₃ films with an additional PMMA encapsulation layer beneath the perovskite layer, thus resulting in dual PMMA-encapsulated pristine MAPbI₃ films.

3.5.1 Preparation of MAPbI₃ Precursor Solution

The precursor solution for MAPbI₃ was prepared by utilizing MAI, PbI₂, DMSO and DMF. To produce the precursor solution, 461 mg of PbI₂ and 159 mg of MAI were put inside a glovebox to be weighed using an analytical balance. To

reduce the interactivity with oxygen and moisture in the surrounding air, they were immediately dissolved in 100 μL DMSO and 900 μL DMF (1:9 ratio) after being transferred out of the glovebox. After that, to prevent further interaction with light, stirring was performed on the precursor solution in the dark for 1 hour. Then, to ensure that the precursor solution is free from any solid impurities, a 0.2 μm PTFE syringe was used to filter the solution.

3.5.2 Preparation of Second PMMA Solution for Dual PMMA Encapsulation

To obtain PMMA solution for the purpose of PMMA encapsulation, commercial acrylic sheets were utilized. Firstly, a vertical saw machine was utilized to cut the acrylic sheets into pieces, which after the pieces underwent a cleaning process through the utilization of ultrasonication. The cleaning process was done so by utilizing dish detergent solution and filtered water whereby each process takes 10 minutes each. After that, a hot plate was utilized to fully dry the pieces at 150 $^{\circ}\text{C}$ for 2 minutes. Then, to produce a PMMA solution with a concentration of 1 mg/ mL, the acrylic pieces were dissolved in ethyl acetate in a closed container at 60 $^{\circ}\text{C}$, followed by vigorous stirring to ensure complete dissolution. After that, the same steps in Section 3.2 were performed.

3.5.3 Deposition of MAPbI_3 and Dual PMMA Encapsulation Layers

Before the deposition of MAPbI_3 layer, an additional PMMA encapsulation layer was formed through the deposition of 100 μL of 1 mg/mL PMMA solution by spin-coating at 4000 rpm for 30 seconds using a pipette tip. After that, the film was heated at 100 $^{\circ}\text{C}$ for 5 minutes.

Then, in the centre of the cooled substrate, 60 μL of the MAPbI_3 precursor solution was spin-coated at 4000 rpm for 10 seconds. Then, the spin-coated film is immediately placed in the vacuum chamber for VASP for 10 seconds to induce more uniform and homogeneous film. After that, further annealing was performed on the film using a hot plate for 5 minutes at 100 $^{\circ}\text{C}$, which resulted in the formation of a dark brown transparent film.

Beyond that, the same steps were repeated to form another PMMA encapsulation layer above the MAPbI₃ layer with the only difference being the concentration of PMMA solution used, i.e., 10 mg/mL of PMMA solution.

3.5.4 Characterizations

For physical appearance assessment, pictures of the samples were taken for every 0, 1, 2, 3 and 5 hours of thermal stressing. SEM (Hitachi S-3400 N), a type of scanning electron microscope, was used to examine the morphologies of the films. The settings for the SEM analysis were set at 5 kV acceleration voltage with 30 μ A probe current. Furthermore, without removing the PMMA layer, an XRD (Shidmazu XRD-6000, Cu K α radiation) investigation was performed to ascertain the phases present in the film. Then, to obtain the peak intensity ratio of PbI₂ to MAPbI₃, the integrated intensity counts of PbI₂ at 12.6° were divided by the integrated intensity counts of MAPbI₃ at 14.1°. Finally, an UV-Vis spectrophotometer (Cary 100) was used to measure the absorbance spectra of the films after every heating allocated time before the samples are taken back for heating.

3.6 Summary

In summary, two methods were used to deposit the PMMA-MAPbI₃ films, i.e., VASP and antisolvent method. In this study, the amount of PMMA additives was manipulated to thoroughly investigate their thermal stability strengthening effect on the MAPbI₃ layer. Besides that, an additional layer of PMMA encapsulation was added to test its effect on the thermal stability of MAPbI₃ films. To identify the presence of thermal degradation, sample characterizations were performed through SEM, XRD and UV-Vis spectroscopy analyses.

CHAPTER 4

RESULTS AND DISCUSSION

4.1 Introduction

This chapter discusses the results obtained using various sample characterization methods as part of the investigation towards the thermal stability enhancement of PMMA as an additive and as encapsulation layers in MAPbI₃ films. To investigate the effect of PMMA additives on the thermal stability of MAPbI₃ films, physical appearance and XRD analyses were carried out on both samples produced using VASP and antisolvent methods. Next, to investigate and compare the effect of PMMA as single and dual encapsulation layers towards the thermal stability of MAPbI₃ films, physical appearance, XRD, UV-Vis and SEM analyses were carried out. Then, the thermal stability enhancement mechanism of PMMA as additives and encapsulation layers will be discussed. For physical appearance analysis, the colour change from dark brown to yellow will signify thermal degradation. For XRD analysis, the peak intensity ratio of PbI₂ to MAPbI₃ will be observed to determine the rate of thermal degradation. For UV-Vis analysis, the change in the absorbance spectra of the film will be observed as part of the method to identify signs of degradation regarding the quality of the films. Last but not least, SEM analysis will observe the morphology changes in the films to investigate the degree of thermal degradation which can be depicted by the formation of pin-holes and PbI₂ needle grains.

4.2 PMMA-Encapsulated Samples Incorporated with PMMA Additives with Vacuum-Assisted Solution Process (VASP) and Antisolvent Method

VASP is a method for depositing thin films of materials onto substrates. In this case, the spin-coated PMMA-MAPbI₃ films were immediately placed in the vacuum chamber before applying vacuum to remove any trapped air or gas bubbles from the spin-coated layer. This method helps to remove gas bubbles

and other impurities from the PMMA-MAPbI₃ layer, resulting in a more uniform and homogeneous film.

4.2.1 Physical Appearance Analysis of PMMA-Encapsulated Samples Incorporated with PMMA Additives with VASP and Antisolvent Method

The physical appearance of the films annealed at 150 °C with VASP is shown in Figures 4.1, 4.2, 4.3, 4.4 and 4.5.

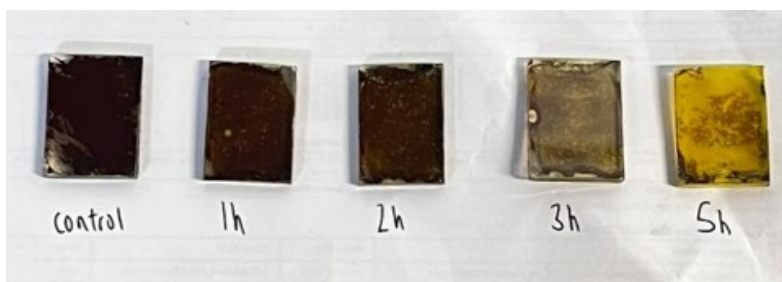


Figure 4.1: Pristine Samples with VASP Annealed at 150 °C for Various Hours.

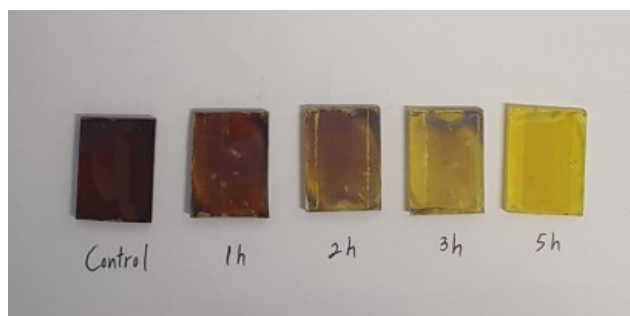


Figure 4.2: Samples Incorporated with 1 mg of PMMA Additives with VASP Annealed at 150 °C for Various Hours.

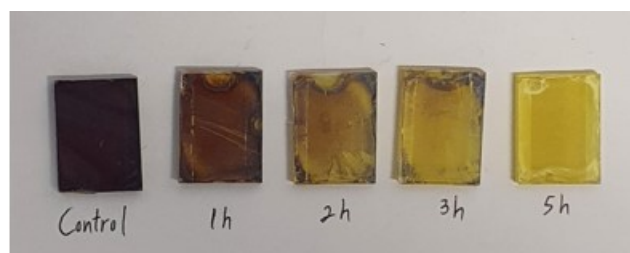


Figure 4.3: Samples Incorporated with 3 mg of PMMA Additives with VASP Annealed at 150 °C for Various Hours.

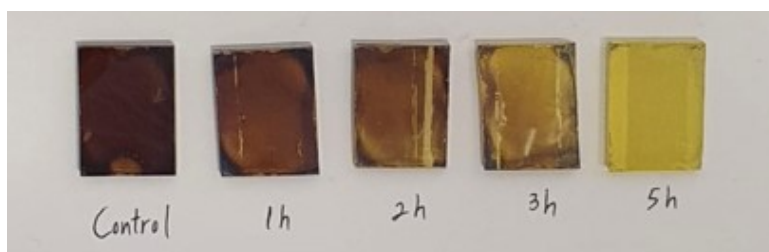


Figure 4.4: Samples Incorporated with 5 mg of PMMA Additives with VASP Annealed at 150 °C for Various Hours.

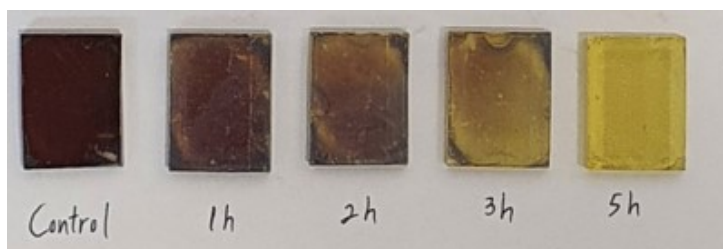


Figure 4.5: Samples Incorporated with 7 mg of PMMA Additives with VASP Annealed at 150 °C for Various Hours.

From Figure 4.1 to 4.5, it can be seen that all the colour of the film samples turns from dark brown to yellow upon annealing due to the thermal degradation of the perovskite samples. As mentioned previously, the dark brown colour represents the MAPbI_3 colour while the formation of PbI_2 is represented by the bleaching of the dark brown films into yellow. Judging from the physical appearance of the PMMA-encapsulated pristine samples in Figure 4.1, the film can still retain the obvious dark brown colour of the MAPbI_3 for the first 2 hours. However, once the annealing time reaches 3 hours, the pristine samples started to show signs of bleaching. This result matches the results reported by Soo et al. (2021) whereby their PMMA-encapsulated films also started to show obvious signs of degradation after 3 hours of annealing. The difference in bleaching intensity between the PMMA-encapsulated films and the samples from Soo et al. (2021) may be explained by the different concentrations and amounts of MAPbI_3 used for spin-coating. Nonetheless, the obvious yellow variation in colour starts to appear once the annealing time reaches 5 hours.

On the other hand, the PMMA-encapsulated MAPbI_3 films that are incorporated with PMMA additives tend to show faster signs of thermal degradation than the pristine samples. In contrast to the pristine samples, the

samples incorporated with PMMA additives already experienced thermal degradation after only 1 hour of annealing as shown by the noticeable yellow PbI_2 spots on the film. The yellow spots can be seen to be the most apparent for the samples with the least amount of PMMA additives added (1 mg) when compared to the other samples with higher amount of PMMA additives added. As observed from the physical appearances in Figures 4.1 to 4.5, after 5 hours of annealing, the samples incorporated with PMMA additives were fully bleached from dark brown into yellow, whereas the pristine samples were still able to retain some dark brown portions on their films. Besides that, it was observed that the higher the amount of PMMA additives added to the MAPbI_3 films, the slower is the bleaching rate and thus the higher the thermal stability of the samples. This speculation is made by observing the samples after 2 hours of annealing whereby the samples with 7 mg of PMMA additives added were able to retain most of the dark brown colour when compared to the others. Therefore, this observation might speculate the thermal stability enhancement potential of PMMA additives. Nonetheless, the PMMA additive-incorporated samples for this case are still visibly less thermally stable than the pristine samples. This result may be due to the incomplete incorporation of PMMA additives as PMMA was immediately precipitated out and condensed into white floccule when the PMMA solution (dissolved in DMF and DMSO solvent) was added into the perovskite precursor solution. This outcome is similar to the results reported by Jia et al. (2017) whereby white floccule also formed when their PMMA solution was added to the perovskite precursor solution as shown in Figure 4.6.



Figure 4.6: Suspension of White Floccule in the Perovskite Precursor Solution (Jia et al., 2017).

To ensure the full incorporation of PMMA additives in MAPbI₃ films, a different method was utilized, i.e., the antisolvent method. Figures 4.7, 4.8, 4.9 and 4.10 show the physical appearance of the films annealed at 150 °C with the antisolvent method. Similar to the results using VASP, the samples from the antisolvent method also showed signs of weaker thermal stability than the pristine samples as seen by the faster bleaching of PMMA-incorporated MAPbI₃ films in Figures 4.7 to 4.9. However, this observation is in contrast with the samples incorporated with 0.15 wt% of PMMA additives, whereby they seem to exhibit stronger thermal stability due to the slower bleaching rate as shown in Figure 4.10. From this, speculations can be made whereby 0.15 wt% or more of PMMA additives incorporated may further enhance the thermal stability of MAPbI₃ films. Besides that, the slower bleaching rate for the samples with the antisolvent method when compared to the VASP samples can be explained by the different concentrations of MAPbI₃ used, in which the antisolvent method used a higher concentration of MAPbI₃ to spin-coat the films. Thus, this results in the slower bleaching rate of films as shown in Figures 4.7 to 4.10. With a different method that enables the full incorporation of PMMA additives, different physical appearance results were obtained which amplified the potential of PMMA additives as a thermal stability enhancer for MAPbI₃ films.

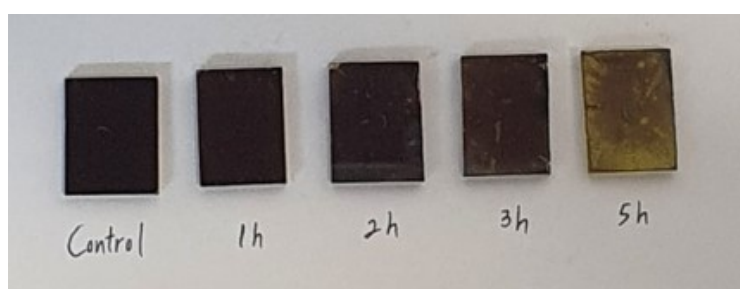


Figure 4.7: Pristine Samples with Antisolvent Method Annealed at 150 °C for Various Hours.

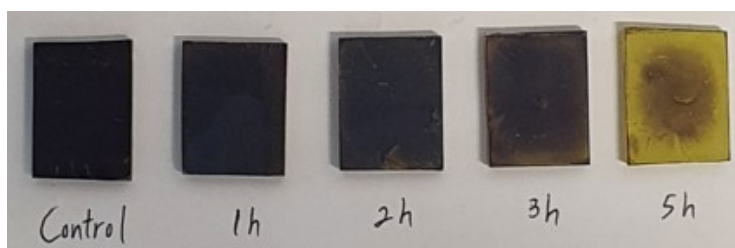


Figure 4.8: Samples Incorporated with 0.05 wt% of PMMA Additives with Antisolvent Method Annealed at 150 °C for Various Hours.

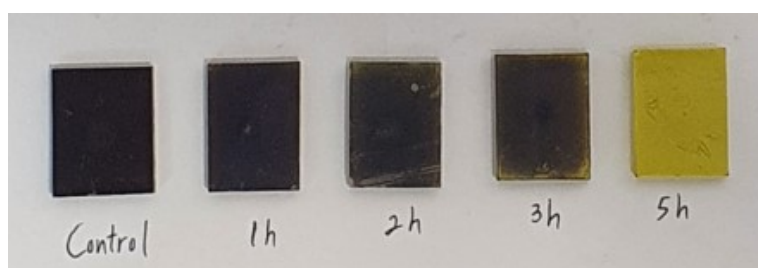


Figure 4.9: Samples Incorporated with 0.10 wt% of PMMA Additives with Antisolvent Method Annealed at 150 °C for Various Hours.

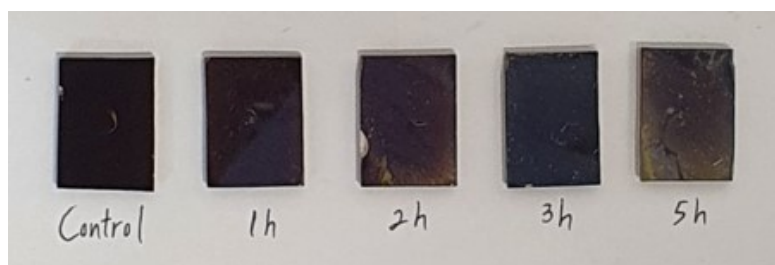


Figure 4.10: Samples Incorporated with 0.15 wt% of PMMA Additives with Antisolvent Method Annealed at 150 °C for Various Hours.

4.2.2 XRD Analysis of PMMA-Encapsulated Samples Incorporated with PMMA Additives with Antisolvent Method

Apart from observing the physical appearances of the samples produced using the antisolvent method, XRD analysis was also conducted to further verify the effect of PMMA additives on the thermal stability of MAPbI₃ films. The XRD results for the antisolvent method are shown in Figures 4.11, 4.12, 4.13 and 4.14.

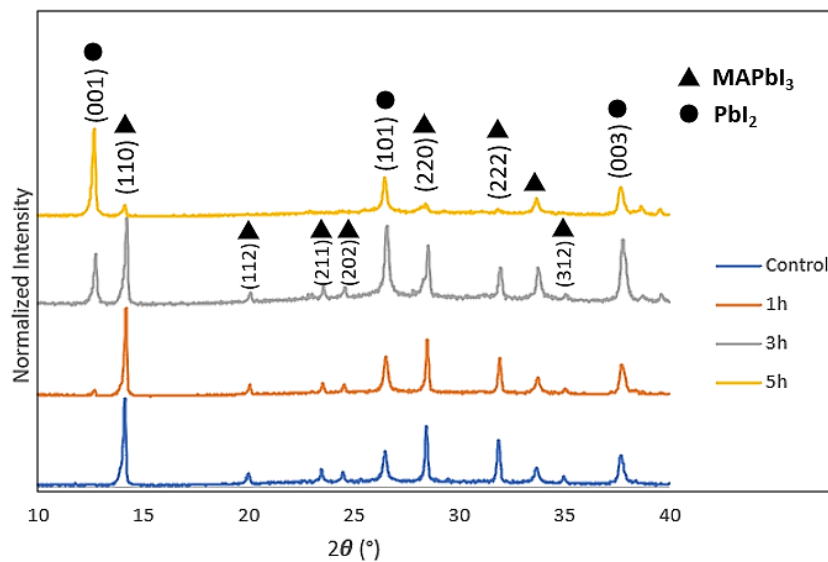


Figure 4.11: XRD Patterns of Pristine PMMA-Encapsulated MAPbI₃ Films using Antisolvent Method Annealed for Various Times.

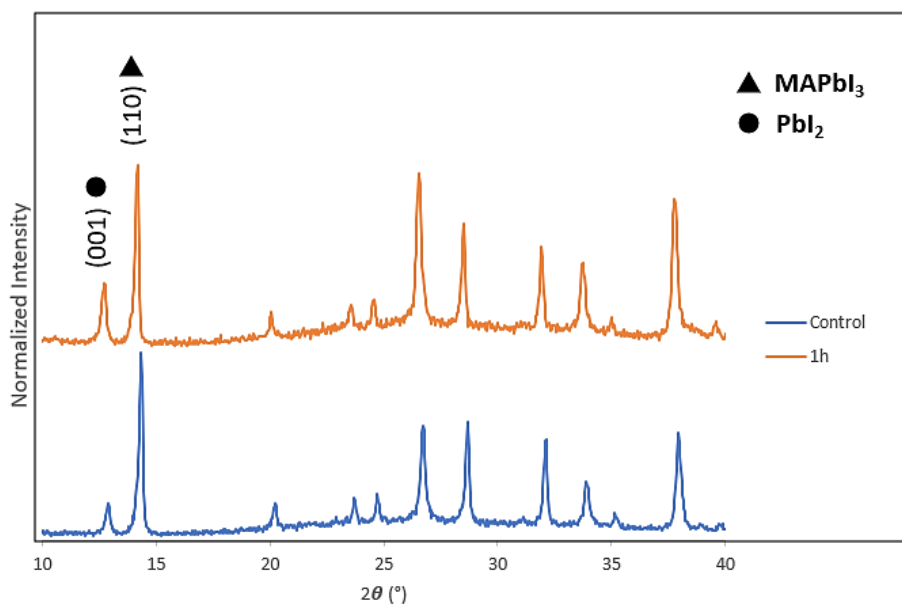


Figure 4.12: XRD Patterns of PMMA-Encapsulated MAPbI₃ Films Incorporated with 0.05 wt% of PMMA using Antisolvent Method Annealed for Various Times.

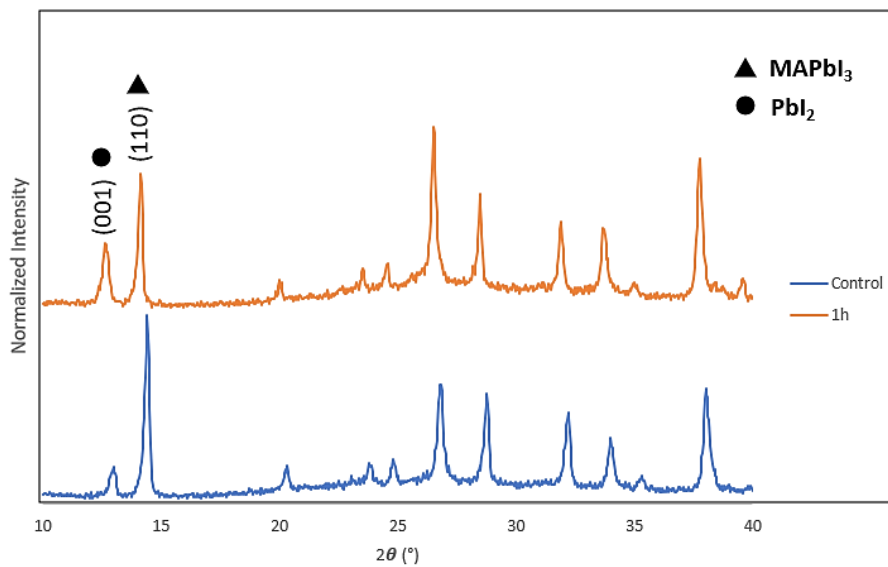


Figure 4.13: XRD Patterns of PMMA-Encapsulated MAPbI₃ Films
Incorporated with 0.10 wt% of PMMA using Antisolvent Method
Annealed for Various Times.

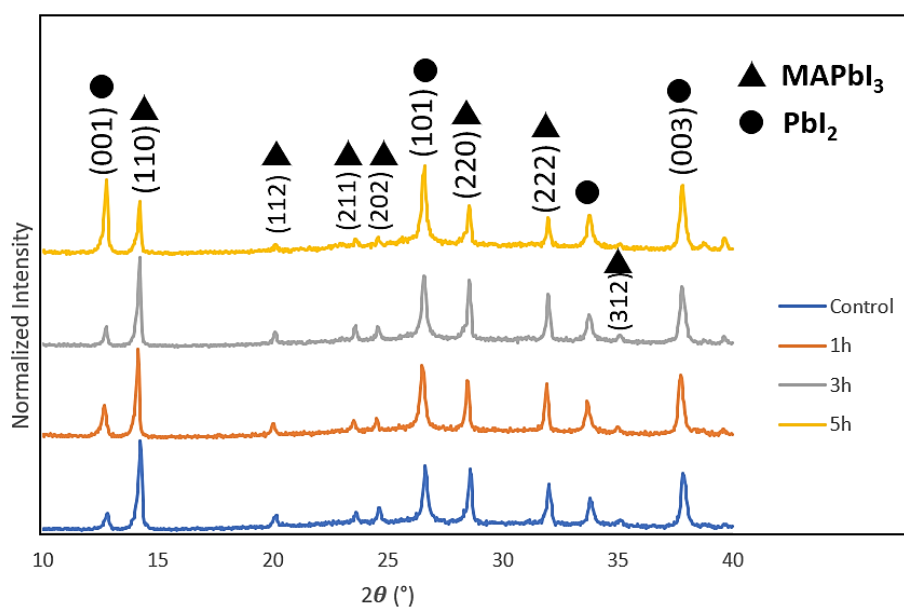


Figure 4.14: XRD Patterns of PMMA-Encapsulated MAPbI₃ Films
Incorporated with 0.15 wt% of PMMA using Antisolvent Method
Annealed for Various Times.

Based on Figure 4.11, it can be seen that the control sample for the pristine samples exhibited pure MAPbI₃ phase with the major typical peaks at 14.1° (110), 28.4° (220) and 31.8° (222) which is in accordance with the work reported by Cheng et al. (2017) and Soo et al. (2021). Besides that, based on the XRD results as shown in Figures 4.11 to 4.14, only a tiny PbI₂ peak at the scattering angle of 12.6° (001) plane can be seen for the pristine samples after 1 hour of annealing while for the samples incorporated with PMMA additives, a huge PbI₂ peak can be observed at the scattering angle of 12.6° even after only 1 hour of annealing, thus signifying the severe thermal degradation of the MAPbI₃ films incorporated with PMMA additives. Not only that, for the samples incorporated with PMMA additives, it can be observed that there is already a PbI₂ peak at 12.6° for the control samples even before going through the annealing process. In this context, it was reported by Jia et al. (2017) whereby his samples underwent a long annealing time for colour transition and crystallization by utilizing the antisolvent method, in which the perovskite film is post-treated with the PMMA solution. The illustration is shown in Figure 4.15 whereby the perovskite films with PMMA incorporated required 150 minutes of annealing time at a temperature of 95 °C in order for the perovskite films to turn fully dark brown, thus signifying full crystallization of the perovskite layer.

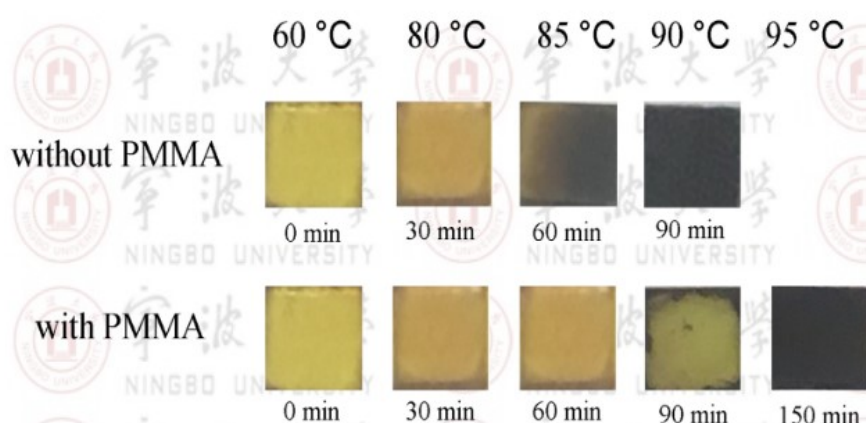


Figure 4.15: The Annealing Time and Temperature on the Colour Transition of the Perovskite Films with and Without PMMA (Jia et al., 2017).

In contrast, this experiment for the antisolvent method was conducted with an annealing time of only 5 minutes at 150 °C. Thus, the huge difference in

annealing time may be the factor that causes the existing minor PbI_2 peak at 12.6° for every sample incorporated with PMMA additives as shown in Figures 4.12 to 4.14 as it was also stated that PMMA polymer can retard the crystallization of perovskite (Jia et al., 2017). Besides that, the XRD patterns from Figure 4.16 shows the gradual crystallization of the MAPbI_3 phase as seen by the decrease in the PbI_2 peak at 12.6° , followed by the increase in MAPbI_3 peak at 14.1° as indicated by the (110) plane when the annealing time increases from 30 to 120 minutes.

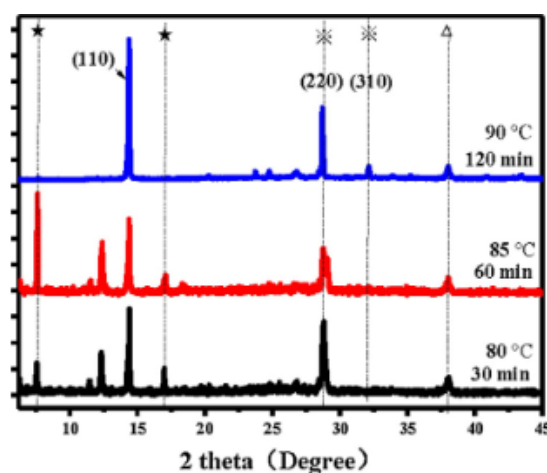


Figure 4.16: XRD Patterns of Perovskite Films with PMMA Evolved with Annealing Time (Jia et al., 2017).

Although the samples incorporated with PMMA additives tend to thermally degrade faster than the pristine samples, the XRD result for the MAPbI_3 films that were incorporated with 0.15 wt% of PMMA additives tend to prove otherwise when the samples were thermally annealed for 3 hours and above. Based on Figure 4.14, it can be seen that the graph exhibited a lower peak intensity ratio of $\text{PbI}_2/\text{MAPbI}_3$ when compared to the pristine samples. This result also matches the physical appearance results from Figure 4.10 whereby the MAPbI_3 films incorporated with 0.15 wt% of PMMA additives were able to retain more dark brown variations than the pristine samples. Besides that, it can be seen that the higher the wt% of PMMA additives added, the higher the ability of the MAPbI_3 films to retain their MAPbI_3 phase. This speculation is supported by the values of the peak intensity ratio of PbI_2 peak ($\approx 12.6^\circ$) to MAPbI_3 ($\approx 14.1^\circ$) for the films as shown in Table 4.1. From Table

4.1, it can be seen that after going through 1 hour of annealing, the higher the wt% of PMMA additives added, the lower the peak intensity ratio of PbI_2 peak to MAPbI_3 for the additive-incorporated films, with the only exception being the samples with the incorporation of 0.10 wt% of PMMA additives. This exception may be due to ever-changing environmental factors such as the humidity of the surrounding area and so on. Since perovskite films are known to be sensitive towards light, moisture, heat and other various external factors, the possibility of a high humidity affecting the degradation of the samples cannot be fully eliminated as the spin-coating process was done in a fume hood that utilizes outside air for ventilation. Apart from that, there may be potential liquid droplets around the spin-coater which remained visibly hard for the naked eye to spot. As mentioned in Section 2.4.1, it was stated that the MA^+ cations of MAPbI_3 are highly hygroscopic, meaning that it tends to absorb moisture from the air, thus allowing moisture to easily break down the structure of MAPbI_3 (Cao et al., 2015). Furthermore, Kim et al. (2019) stated that their PMMA-encapsulated MAPbI_3 films degraded within 6 minutes of water exposure as water molecules can hydrolyse the ester groups in PMMA and disassemble the PMMA structure because a portion of the PMMA molecular chain is hydrophilic. Once the PMMA encapsulation layer is disassembled, the perovskite layer will be exposed to the surrounding, leading to further degradation. In a nutshell, after 5 hours of thermal annealing, the peak intensity ratio of PbI_2 peak to MAPbI_3 is significantly lower for the MAPbI_3 films incorporated with 0.15 wt% of PMMA additives when compared to the pristine samples as proven with a value of 1.7577 and 8.6618, respectively. Therefore, all of these results prove that adding a higher amount of PMMA additives may uphold their potential to further enhance the thermal stability of MAPbI_3 films.

Table 4.1: Peak Intensity Ratio of $\text{PbI}_2/\text{MAPbI}_3$ for Antisolvent Perovskite Samples.

Amount of PMMA Additives Added	Peak Intensity Ratio of $\text{PbI}_2/\text{MAPbI}_3$			
	Control	1h	3h	5h
Pristine	0	0.0642	0.7198	8.6618
0.05 wt%	0.1957	0.4635	-	-
0.10 wt%	0.1997	0.6344	-	-
0.15 wt%	0.2494	0.4545	0.2953	1.7577

Regarding the varying effects of PMMA additives on the thermal stability of MAPbI_3 films as seen from the previous results, a lower amount of PMMA additives incorporated may induce a less homogeneous distribution of PMMA in the film, leading to the formation of voids and defects that act as nucleation sites for the degradation of MAPbI_3 under thermal stress, causing the film to exhibit lower thermal stability when compared to pristine films. However, when a higher amount of PMMA is added beyond a certain threshold, or in this case, 0.15 wt%, it can enhance the thermal stability of MAPbI_3 films. This may be due to the formation of a more uniform PMMA matrix within the MAPbI_3 films as a result of the higher concentration of PMMA additives incorporated. By having a more uniform matrix, the formation of defects and voids that promote thermal degradation can be reduced, leading to enhanced thermal stability. Nonetheless, the optimal amount of PMMA additives needed to enhance the thermal stability of MAPbI_3 films may differ based on the different fabrication processes and thermal conditions applied.

4.3 Pristine Samples with Single and Dual PMMA Encapsulation Layers

To confirm the difference in the ability of PMMA as an encapsulation layer and as an additive, pristine samples with dual layers of PMMA encapsulation were produced with VASP method. Then, the results for the characterizations of pristine samples for single and dual layers of PMMA encapsulation were recorded and compared.

4.3.1 Physical Appearance Analysis of Pristine Samples with Single and Dual PMMA Encapsulation Layers

First of all, the physical appearance of the single PMMA-encapsulated pristine MAPbI₃ (S-PMMA-MAPbI₃) and dual PMMA-encapsulated pristine MAPbI₃ (D-PMMA-MAPbI₃) samples was recorded after various hours of annealing as shown in Figure 4.17 and 4.18.

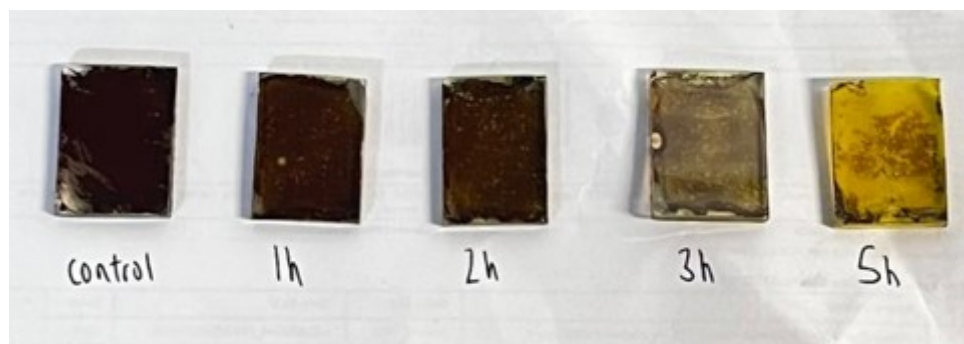


Figure 4.17: Physical Appearance of S-PMMA-MAPbI₃ Films Annealed at 150 °C for Various Hours.

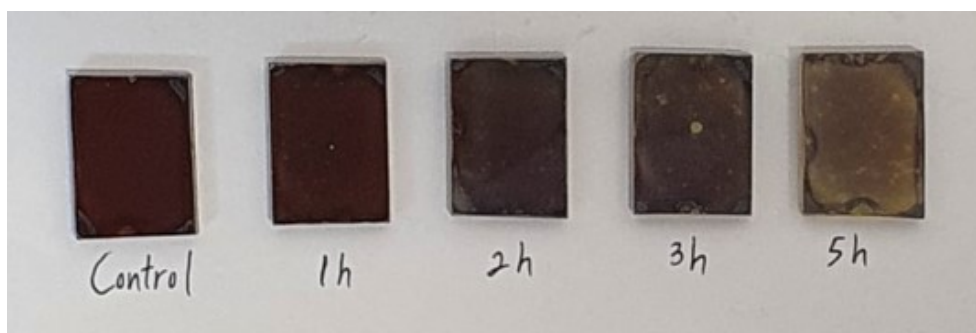


Figure 4.18: Physical Appearance of D-PMMA-MAPbI₃ Films Annealed at 150 °C for Various Hours.

Similar to the previous results, the control for the pristine samples exhibited a dark brown colour appearance with mirror-like reflective properties before going through any thermal annealing. After going through thermal annealing, the dark brown colour of the samples will gradually experience bleaching due to thermal degradation. However, in this case, the pristine samples with dual PMMA encapsulation layer experienced lesser bleaching when compared to the single layer samples as shown by the obvious colour difference in the physical appearance of the films. The visible difference can be

spotted at 1 hour of annealing onwards whereby the S-PMMA-MAPbI₃ samples first exhibited some minor yellow spots among the dark brown appearance for 1 and 2 hours of thermal annealing. On the other hand, the D-PMMA-MAPbI₃ samples were able to retain the dark brown colour appearance with only slight bleaching after 2 hours of thermal annealing. For 3 hours onwards of thermal annealing, the S-PMMA-MAPbI₃ films can be seen to experience a severe thermal degradation as inferred from the intense bleaching of films from dark brown to yellow. In contrast, the D-PMMA-MAPbI₃ films were still visibly dark brown with relatively fewer signs of thermal degradation to yellow PbI₂ that initiated at the edge of the films. Overall, after 5 hours of thermal annealing, the dual PMMA layer samples can still retain most of the dark brown colour appearance with some minor yellow variations while the S-PMMA-MAPbI₃ films exhibited severe colour change from dark brown to yellow. Therefore, judging from the physical appearance results, it can be speculated that the thermal stability of D-PMMA-MAPbI₃ samples surpasses that of the S-PMMA-MAPbI₃ samples.

4.3.2 XRD Analysis of Pristine Samples with Single and Dual PMMA Encapsulation Layers

From the XRD results as shown in Figures 4.19 and 4.20, it can be seen that the control samples exhibit a similar pattern when compared with the previous pristine result that was produced using the antisolvent method whereby the major MAPbI₃ peaks can be seen at 14.1° and 28.4° with the exception of the peak at 31.8°. This may be due to the different deposition methods utilized whereby VASP may have affected the crystal orientation of MAPbI₃.

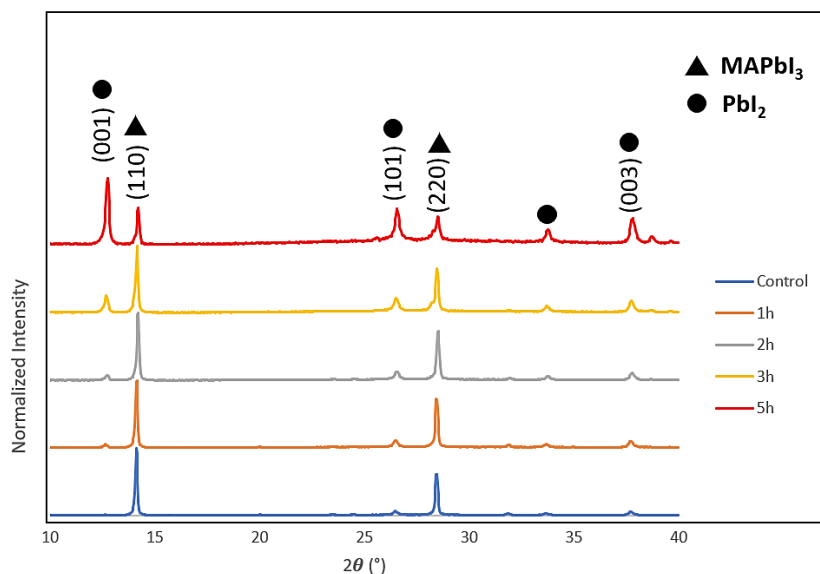


Figure 4.19: XRD Patterns of S-PMMA-MAPbI₃ Films Using VASP Method Annealed at 150 °C for Various Hours.

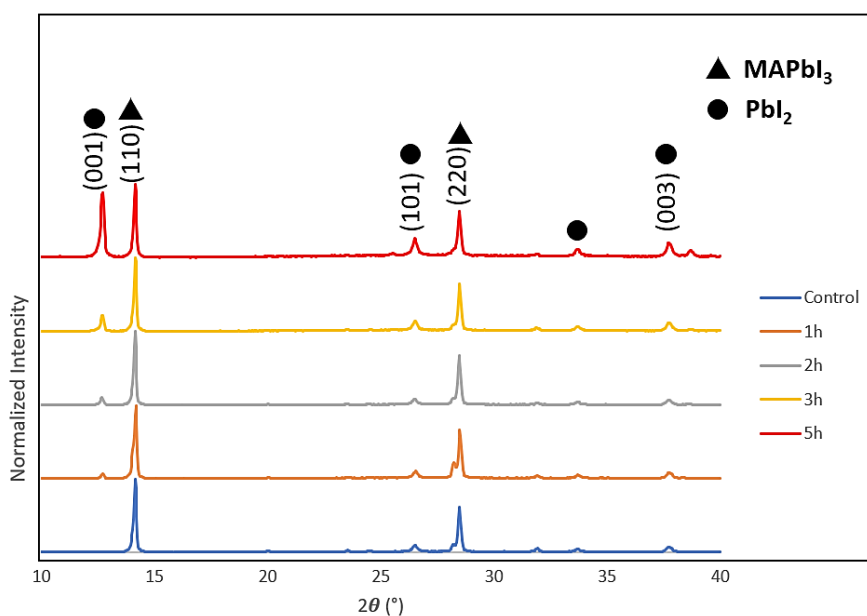


Figure 4.20: XRD Patterns of D-PMMA-MAPbI₃ Films Using VASP Method Annealed at 150 °C for Various Hours.

Besides that, both of the XRD results from Figure 4.19 and 4.20 exhibited the same characteristics whereby the longer the duration of thermal annealing, the higher is the PbI₂ peak at (001) plane, thus signifying the thermal degradation of MAPbI₃ into PbI₂. After 1 hour of thermal annealing, it can be seen that both the single and dual PMMA-encapsulated samples exhibited a minor peak at (001)

plane which is in accordance with the XRD results for single PMMA-encapsulated pristine samples from Soo et al. (2021). This explains the slight yellow variations spotted in the physical appearance of the samples for the first hour of annealing. For the D-PMMA-MAPbI₃ samples, although no obvious yellow variations can be seen from the naked eye, the XRD results from Figure 4.20 confirms the initiation of thermal degradation upon the first hour of thermal annealing. As the duration of thermal annealing proceeds to 5 hours, a major difference can be spotted between the two results whereby for the S-PMMA-MAPbI₃, the PbI₂ peak at (001) plane completely dominated the MAPbI₃ peak at (110) plane. On the other hand, the MAPbI₃ peak at (110) plane is still visibly higher than the PbI₂ peak at (001) plane for the D-PMMA-MAPbI₃ samples. This result proves that D-PMMA-MAPbI₃ samples exhibited stronger thermal stability than S-PMMA-MAPbI₃ samples. It is also worth noting that a new PbI₂ peak can be observed at 38.6° for both of the XRD results when the thermal annealing duration reached 5 hours. Furthermore, Table 4.2 shows that the peak intensity ratio of PbI₂/MAPbI₃ of S-PMMA-MAPbI₃ exceeded that of the D-PMMA-MAPbI₃ samples by a significant amount, thus further signifying the thermal stability improvement by adding another layer of PMMA encapsulation underneath the perovskite layer. Moreover, for every duration of thermal annealing, the S-PMMA-MAPbI₃ samples exhibited a higher peak intensity ratio of PbI₂/MAPbI₃ than the D-PMMA-MAPbI₃ except for 2 hours. The exception may be due to the plausibility of the sample being equipped with less effective PMMA encapsulation layers as a result of human errors during the spin-coating process. With lesser coverage of PMMA encapsulation, the perovskite layer will be more exposed to the outer environment and thus further degradation of MAPbI₃ to PbI₂ will be induced, leading to a higher peak intensity ratio of PbI₂/MAPbI₃.

Table 4.2: Peak Intensity Ratio of $\text{PbI}_2/\text{MAPbI}_3$ for Single and Dual PMMA-Encapsulated Perovskite Samples.

Amount of PMMA Encapsulation Layers	Peak Intensity Ratio of $\text{PbI}_2/\text{MAPbI}_3$				
	Control	1h	2h	3h	5h
Single	0	0.0742	0.1144	0.3866	2.4087
Dual	0	0.0656	0.1200	0.2754	1.0936

4.3.3 UV-Vis Spectroscopy Analysis of Pristine Samples with Single and Dual PMMA Encapsulation Layers

UV-Vis spectroscopy analysis was also conducted on both the S-PMMA- MAPbI_3 and D-PMMA- MAPbI_3 samples as UV-Vis spectroscopy is a useful analytical tool for determining the thermal stability of a substance because changes in the electronic structure of a molecule as a result of thermal degradation can be detected through changes in the UV-Vis absorption spectra.

When a substance undergoes thermal degradation, its molecular structure can change, resulting in changes in the electronic transitions that occur in the UV-Vis region. These changes can be detected by measuring the UV-Vis absorption spectrum of the substance before and after thermal annealing. Typically, the UV-Vis absorption spectrum of a substance will have a characteristic pattern of absorption peaks at specific wavelengths. In this case, as the duration of thermal annealing increases, the intensity of these peaks may decrease or shift in wavelength, indicating that the electronic transitions in the molecule are changing due to thermal degradation.

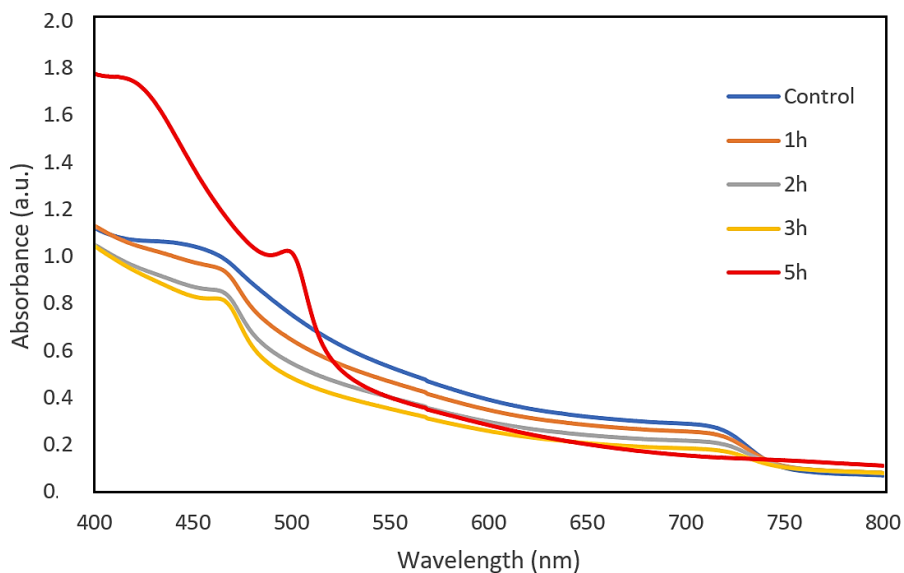


Figure 4.21: UV-Vis Spectra of S-PMMA-MAPbI₃ Films.

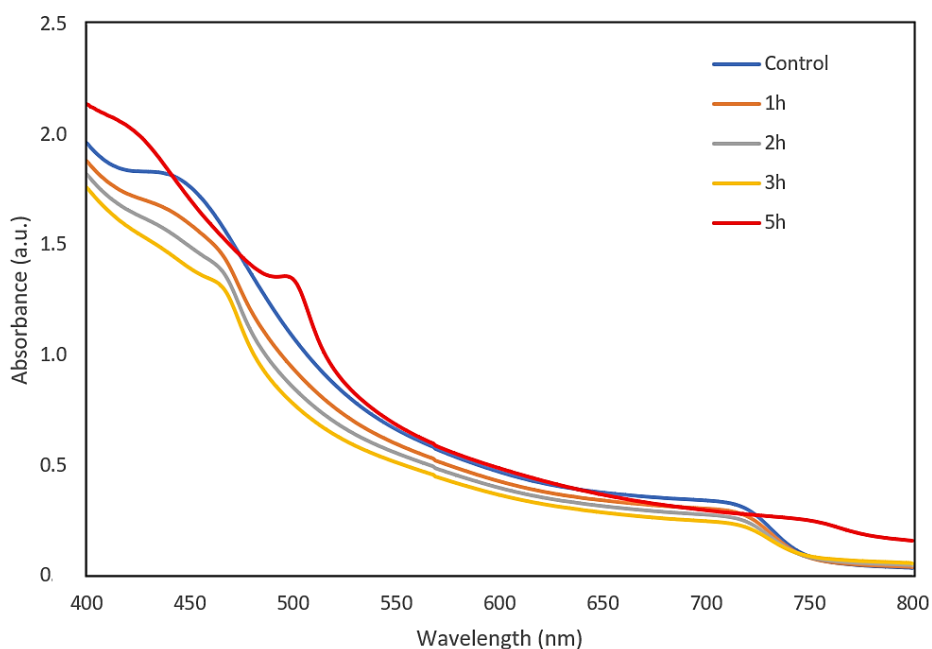


Figure 4.22: UV-Vis Spectra of D-PMMA-MAPbI₃ Films.

Besides that, based on Figures 4.21 and 4.22, the UV-Vis spectra of both S-PMMA-MAPbI₃ and D-PMMA-MAPbI₃ samples exhibited similar MAPbI₃ and PbI₂ peaks at the wavelength of around 725 nm and 500 nm, respectively which is similar with the works reported by Yang et al. (2015), Dualeh et al. (2014) and Soo et al. (2021). The slight difference in the wavelengths between this work and the previously reported works may be due

to the thermal decomposition of MAPbI₃ which leads to a shift in the band edge. Apart from that, it can be seen that the longer the duration of thermal annealing, the lower is the absorbance for 400 nm to 750 nm with the UV-Vis absorption spectrum for 5 hours being an exception. The decrease in absorbance signified thermal degradation as the molecular structure of a substance tends to change upon thermal degradation, thus altering the substance's ability or in this case, MAPbI₃, to absorb light at specific wavelengths. This statement is also supported by Figure 4.23 which shows the lower absorbance of pure PbI₂ films when compared to MAPbI₃ films. On the other hand, the abnormally higher absorbance for the samples that underwent 5 hours of thermal annealing may be due to the higher levels of Mie scattering within the film, stipulating that large crystallites are formed as part of the thermal decomposition process, thus giving the false impression of a higher absorbance (Yang et al., 2015).

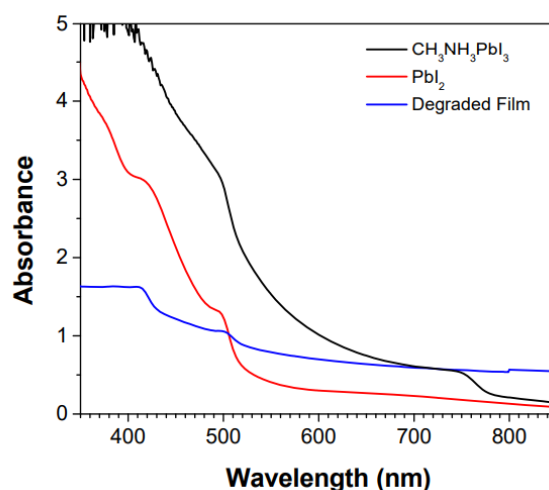


Figure 4.23: UV-Vis Absorption Spectra of Pristine MAPbI₃, Pure PbI₂ and Degraded MAPbI₃ Film (Yang et al., 2015).

Other than that, based on Figures 4.21 and 4.22, more apparent signs of thermal degradation can be noted starting from 1 hour of thermal annealing for S-PMMA-MAPbI₃ films when compared to D-PMMA-MAPbI₃ films. This is inferred from the 1-hour and 2-hour UV-Vis absorption spectra whereby a clearer peak at around 470 nm is manifested for S-PMMA-MAPbI₃ when compared to D-PMMA-MAPbI₃. Starting from 3 hours of thermal annealing,

both the absorption spectra of the S-PMMA-MAPbI₃ and D-PMMA-MAPbI₃ samples exhibited more severe peaks which are in contrast with that of the control samples. In addition, for 5 hours of thermal annealing, a huge peak of the PbI₂ band edge can be observed at 500 nm for both S-PMMA-MAPbI₃ and D-PMMA-MAPbI₃ samples with a bigger peak for S-PMMA-MAPbI₃ samples. Furthermore, the MAPbI₃ band edge at 725 nm starts to flatten out after 5 hours of thermal annealing for both categories of samples. Nonetheless, the flattening of the MAPbI₃ band edge is still visibly more apparent for S-PMMA-MAPbI₃ samples, thus signifying the superior thermal stability of D-PMMA-MAPbI₃ samples. These results match the physical appearance and XRD results from Figures 4.17 to 4.20, especially for the significantly higher peak intensity ratio of PbI₂/MAPbI₃ for S-PMMA-MAPbI₃ which demonstrated the slower signs of thermal degradation of D-PMMA-MAPbI₃ samples.

4.3.4 SEM Analysis of Pristine Samples with Single and Dual PMMA Encapsulation Layers

SEM analysis was also conducted to study the changes in morphology before and after thermal annealing, together with the comparison between D-PMMA-MAPbI₃ and S-PMMA-MAPbI₃ films.

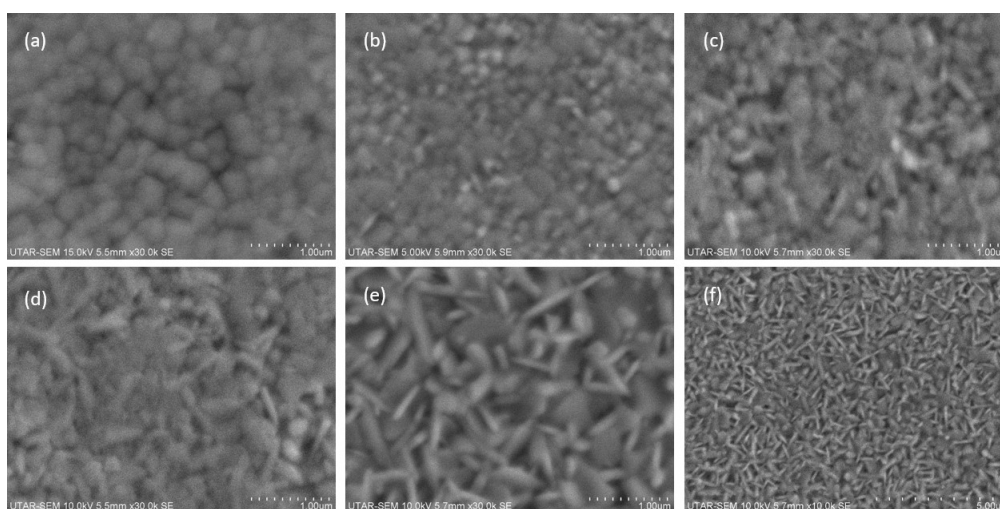


Figure 4.24: SEM Images of S-PMMA-MAPbI₃ Film Annealed for Various Times: (a) Control, (b) 1 h, (c) 2 h, (d) 3 h, (e) 5 h and (f) 5 h (Lower Magnification).

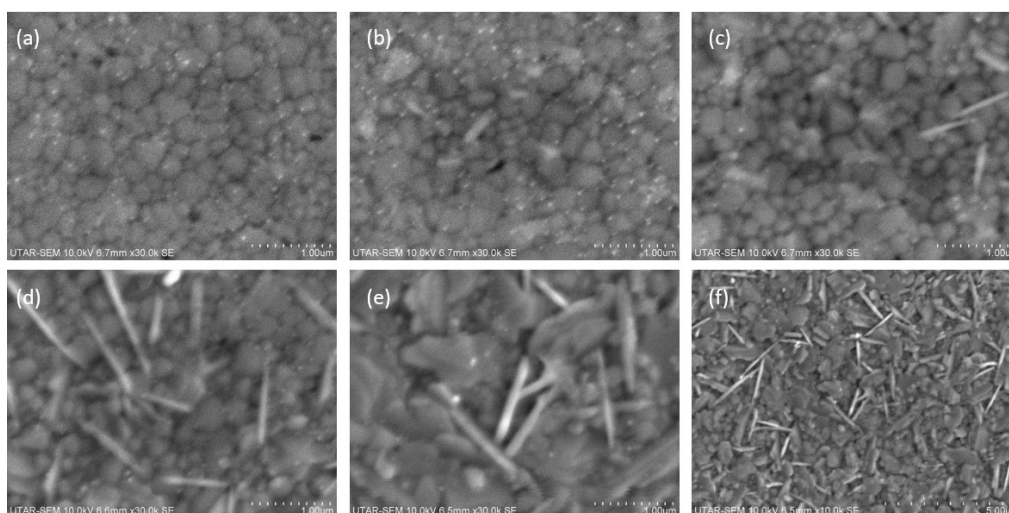


Figure 4.25: SEM Images of D-PMMA-MAPbI₃ Film Annealed for Various Times: (a) Control, (b) 1 h, (c) 2 h, (d) 3 h, (e) 5 h and (f) 5 h (Lower Magnification).

Based on the SEM results from Figures 4.24 and 4.25, it can be seen that the morphology of both the S-PMMA-MAPbI₃ and D-PMMA-MAPbI₃ films exhibited similar characteristics with increasing hours of thermal annealing. The first characteristic is the enlargement of the grain size while the second is the formation of PbI₂ needles which is in accordance with the results reported by Soo et al. (2021). However, the increase of the grain size only proceeded until 2 hours of thermal annealing before the amount of PbI₂ needle grains start to manifest abundantly. In fact, for both S-PMMA-MAPbI₃ and D-PMMA-MAPbI₃ films, a rod-like structure can be seen to appear in minority at 1 hour of thermal annealing as shown in Figure 4.24 (b) and Figure 4.25 (b). This result is in accordance with the XRD results whereby tiny PbI₂ peaks at the scattering angle of 12.6° can be noted for both categories of samples, signifying the initiation of a minor thermal degradation. Besides that, the white spots that were spotted in Figure 4.25 (a) and (b) may be attributed to the presence of moisture or any unwanted dust particles that were induced during the process of sample characterizations as these processes involved subsequent taking in and out of samples from the glovebox, therefore exposing the samples to the outer environment. The increase in grain size is caused by Ostwald recrystallization which involves two steps. The first step involves the dissolution of small-sized crystals while the second step involves the formation of large-sized crystals for

the purpose of reducing surface energy at elevated temperatures of 100 °C and above. The illustration of Ostwald recrystallization is shown in Figure 4.26. Besides that, the cracks and voids formed after thermal annealing could also be attributed to Ostwald recrystallization (Huang et al., 2018).

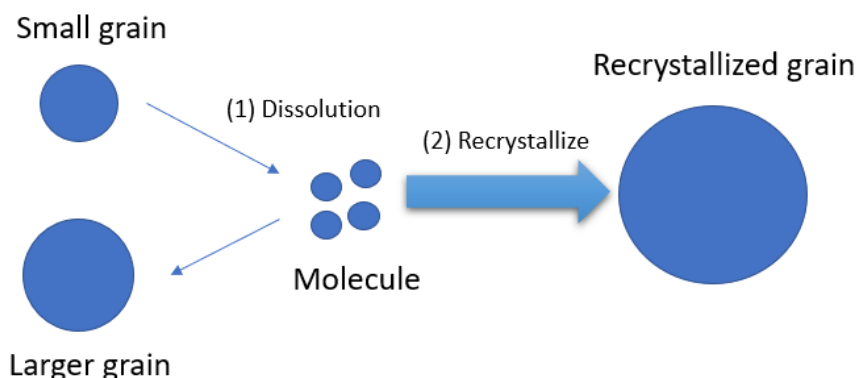


Figure 4.26: Illustration of Ostwald Recrystallization (Huang et al., 2018).

The Ostwald recrystallization process also explains the presence of large and small grain clusters in 1 and 2 hours of thermal annealing as the small grains are being consumed to form larger grains. This explains the increment of grain size from the control samples to 2 h samples as shown in Table 4.3. Once the thermal annealing reaches 3 hours, more PbI_2 needle grains can be seen for both the categories of samples, followed by the decrease in grain size as thermal degradation of MAPbI_3 films will cause its grain size to decrease. Needless to say, 5 hours of thermal annealing shows the most amount of PbI_2 needles due to severe thermal decomposition of MAPbI_3 .

Apart from that, pin-holes and the fusing of GBs can also be seen in both 5 hours samples (Figures 4.24 (f) and 4.25 (f)) which can be attributed to the escape of volatile MAI from MAPbI_3 . The remaining PbI_2 was then reported to fuse the remaining MAPbI_3 grains (Li et al, 2017; Soo et al., 2021). The fusing of GBs explains why the grain size is larger for 5 h samples. Furthermore, a major difference that can be spotted between the two categories of samples is the sheer amount of PbI_2 needles spotted in S-PMMA- MAPbI_3 film when compared to D-PMMA- MAPbI_3 film for 5 hours of thermal annealing. This result matches the previous sample characterization results in which the S-

PMMA-MAPbI₃ films exhibited more yellow variations (physical appearance result) and a dominant PbI₂ peak at the diffraction peak of 12.6°. The lesser amount of PbI₂ needle grains spotted in D-PMMA-MAPbI₃ films after 5 hours of thermal annealing signifies the stronger thermal stability of having dual PMMA encapsulation layers.

Table 4.3: Average Grain Size of S-PMMA-MAPbI₃ and D-PMMA-MAPbI₃ Films Annealed at Various Hours.

	Average Grain Size (nm)	
	S-PMMA-MAPbI ₃	D-PMMA-MAPbI ₃
Control	235.4	287.4
1 h	271.8	337.5
2 h	304.8	440.4
3 h	248.9	245.1
5 h	312.7	490.3

4.4 Thermal Stability Enhancement Mechanism of PMMA As Additive and Dual Encapsulation Layers

As mentioned in Section 2.4.4, the defect sites at the GBs which comprised of halide vacancies and Pb-halide antisites contributed to the thermal degradation of the MAPbI₃ films. This is because the defects were reported to be the cause for the increment of ion migration as they tend to reduce the activation energy needed for ion migration. Furthermore, as reported previously by both Shao et al. (2016) and Lee et al. (2019), the reduction of activation energy required will induce the ions to migrate to other places, leading to the release of volatile MAI from GBs. Moreover, Soo et al. (2022) reported that thermal annealing may also contribute sufficient energy for the halide ions to move to the defect sites at the GBs which serve as channels for the escape of volatile MAI. In addition, it was stated that charge accumulation between interfaces is what causes perovskite hysteresis. Since this charge accumulation is primarily brought on by ion migration, the more the reason for the suppression of ion migration at the GBs for thermal stability enhancement (Zhao et al., 2021). In this context, the

encapsulation of PMMA on top of the perovskite film can serve as a passivation mechanism towards the defect sites at the GBs of the MAPbI₃ polycrystalline film at the interface between the film and air (Soo et al., 2021).

Besides that, it was reported that polymers with carbonyl groups such as PMMA can act as Lewis base sites whereby the lone pair electrons of the Lewis bases could interact with the under-coordinated Pb atoms at the GBs to form a dipole-ion interaction (Han et al., 2019; Peng et al., 2018). Soo et al. (2021) also illustrated the plausible passivation mechanism whereby the lone pair of electrons in the carbonyl group of PMMA established a coordinative bond with the I vacancy at GBs at the MAPbI₃ film/air interface as shown in Figure 2.9. In this case, an additional layer of PMMA encapsulation was added beneath the MAPbI₃ film. With twice the layers of PMMA passivating the defect sites at the MAPbI₃ film/air and MAPbI₃ film/SnO₂ interface, there will be less ion migration towards the defect sites at the GBs which serve as channels for the escape of volatile MAI. The sample characterization results also match this speculation as shown by the increased thermal stability of D-PMMA-MAPbI₃ films when compared to S-PMMA-MAPbI₃ films. The illustration of the plausible passivation mechanism of dual PMMA encapsulation layers is shown in Figure 4.27.

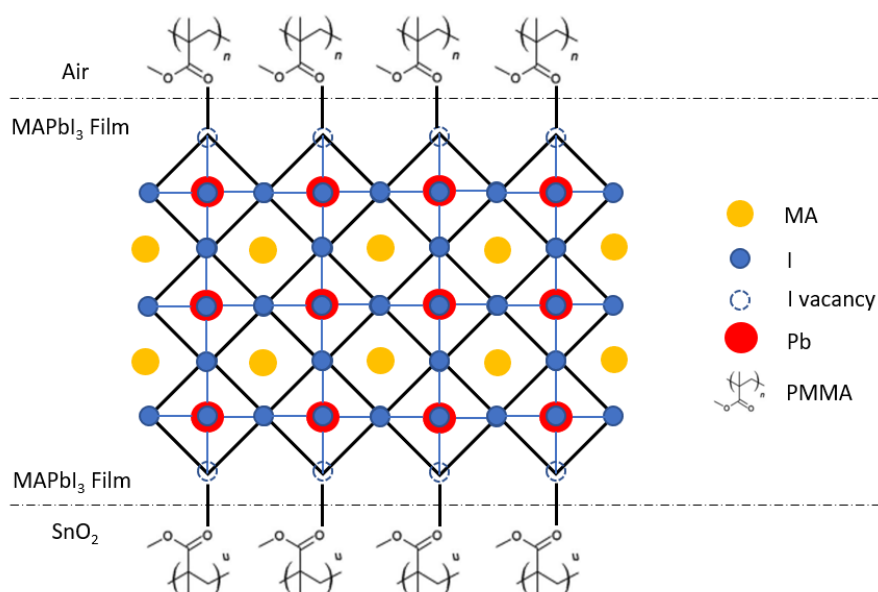


Figure 4.27: Passivation Mechanism on GBs by Dual PMMA Encapsulation Layers Through the Carbonyl Group of PMMA.

As an additive, PMMA should be able to perform the same passivation mechanism by utilizing its carbonyl group to form coordinative bonds with the Pb^{2+} defect sites located at the GBs within the MAPbI_3 film. When incorporated as an additive, PMMA is able to further passivate defect sites within the MAPbI_3 film which is unreachable by the PMMA encapsulation layers as shown in Figure 4.28.

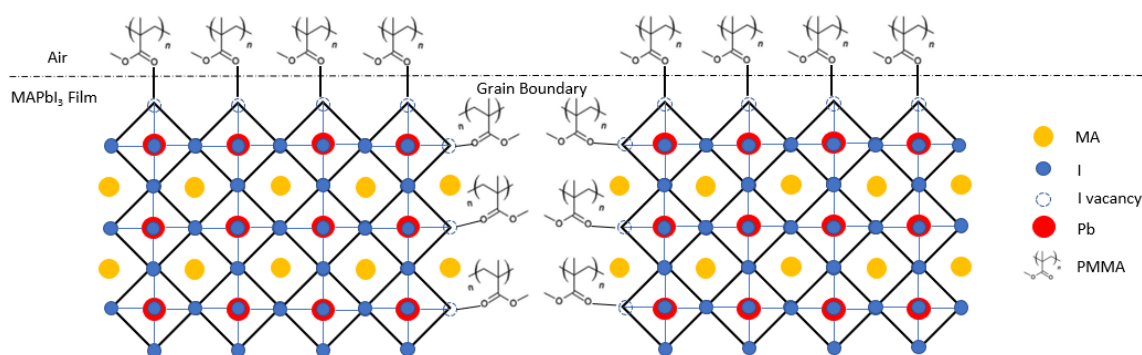


Figure 4.28: Passivation Mechanism on GBs by PMMA Additives Within MAPbI_3 Films.

Furthermore, as mentioned in Section 2.4.5, the addition of PMMA can form an intermediate adduct with PbI_2 , delaying the growth of perovskite crystals which in turn allowed the randomly generated nuclei to modify their orientation and grow in the thermodynamically favourable orientation. Moreover, the addition of PMMA can also reduce the bulk defects in perovskite films (Bi et al, 2016; Jia et al., 2017). In a nutshell, PMMA can be used as both an additive and as encapsulation layers to enhance the thermal stability of MAPbI_3 films. Since the addition of PMMA as an additive was only tested until 0.15 wt%, the further potential of PMMA additive as a thermal stability enhancer to exceed the performance of PMMA as dual encapsulation layers still require further investigation.

4.5 Summary

In summary, PMMA was proven to enhance the thermal stability of MAPbI_3 films by incorporating the polymer as an additive or as encapsulation layers in MAPbI_3 films. In this context, 0.15 wt% of PMMA additives was found to be

the most prominent amount in enhancing the thermal stability of MAPbI₃ films. With that being said, further investigation is still required to investigate whether the increment of PMMA additives above 0.15 wt% will induce further thermal stability enhancement in MAPbI₃ films. Besides that, dual PMMA encapsulation layers with each layer above and beneath the MAPbI₃ layer were found to be more effective in enhancing the thermal stability of MAPbI₃ films when compared to a single layer of PMMA encapsulation. The mechanism behind the thermal stability enhancement of PMMA as an additive and as encapsulation layers is attributed to the function of their carbonyl group to passivate the GBs at the film/air and film/SnO₂ interfaces and also within the films where it is unreachable by the PMMA encapsulation layers.

Overall, it was observed that incorporating PMMA additives and dual PMMA encapsulation layers in MAPbI₃ films can develop better thermal stability when compared to previous works such as Eperon et al. (2014) and Chaudhary et al. (2020) which reported full thermal degradation at 60 minutes and 90 minutes, respectively when there were no PMMA additives and PMMA encapsulation layers added. However, caffeine additives were seen to exhibit stronger thermal stability enhancement effect than PMMA additives. In this context, Soo et al. (2022) reported that the caffeine-incorporated MAPbI₃ films exhibited a peak intensity ratio of PbI₂ to MAPbI₃ of only 0.27 even after 24 hours of thermal stressing which is comparatively much lower than 1.7577 as exhibited by the PMMA-incorporated MAPbI₃ films after only 5 hours of thermal stressing. Nonetheless, the potential of PMMA additives as a thermal stability enhancer has not been fully explored yet as further investigation is still required to study the effects of PMMA additives beyond 0.15 wt%.

CHAPTER 5

CONCLUSIONS AND RECOMMENDATIONS

5.1 Conclusions

In conclusion, the incorporation of PMMA additives and PMMA encapsulation layers has successfully enhanced the thermal stability of MAPbI₃ films. When compared to single PMMA-encapsulated pristine MAPbI₃ films, the dual PMMA-encapsulated pristine MAPbI₃ films exhibited better thermal stability enhancement which may be attributed to the twofold passivation effect towards the GB defects at the film/air and film/SnO₂ interfaces. This statement is also proven by the results from the XRD analyses conducted after 5 hours of thermal stressing whereby the dual PMMA-encapsulated pristine MAPbI₃ films exhibited a lower peak intensity ratio of PbI₂ to MAPbI₃ with the value of 1.0936 when compared to 2.4087 for the single-PMMA encapsulated pristine MAPbI₃ films. On the other hand, PMMA additives also played a similar role by passivating the GB defects within the MAPbI₃ films where it is unreachable by the PMMA encapsulation. For this experiment, the optimum concentration of PMMA additives incorporated is 0.15 wt%. However, the thermal stability strengthening effect of PMMA additives still requires further investigation as it is unsure whether the increment of PMMA additives beyond 0.15 wt% will further enhance the thermal stability of MAPbI₃ films. Nonetheless, the incorporation of 0.15 wt% of PMMA additives into the MAPbI₃ films still exhibited better thermal stability than the pristine MAPbI₃ films after 5 hours of thermal stressing as proven by the significant reduction in peak intensity ratio of PbI₂ to MAPbI₃ from 8.6618 to 1.7577 while supported by other results such as the lower bleaching intensity of the dark brown colour of MAPbI₃ films, the lower formation of PbI₂ needle grains and the retention of MAPbI₃ UV-Vis band edge.

5.2 Recommendations for Future Work

There are a few recommendations that can be considered for future work. One of the recommendations includes implementing the incorporation of both PMMA additives and dual PMMA encapsulation layers in the MAPbI₃ films. With the passivation effect of both PMMA additives and dual PMMA encapsulation layers, the thermal stability of MAPbI₃ films may achieve an even higher stage, thus leading to a higher possibility of manufacturing and commercialization of operationally stable PSCs.

Besides that, with dual PMMA encapsulation layers, only the film/air and film/SnO₂ interfaces are protected from various degradation-inducing factors such as moisture, heat and so on. In this context, the sides of the MAPbI₃ films are not covered with any protective layers at all, which may further induce degradation upon the films. Thus, measures should be taken in future works to ensure that the sides of the MAPbI₃ films are sealed off from various factors that may induce further degradation of the films.

Apart from that, actual metal oxide sols should be applied on top of the MAPbI₃ films to investigate the actual possibility of depositing metal oxide sols as the CTLs of PSCs with enhanced thermal stability. Moreover, since the enhanced thermal stability is only part of the requirement towards the commercialization of PSCs, the performance of solar cells in terms of PCE which can be defined by three factors, namely, J_{SC} , V_{OC} and FF, should also be investigated in future works to identify whether the incorporation of PMMA additives and dual PMMA encapsulation layers will attribute to the increase in PCE or backwards.

REFERENCES

- Aristidou, N., Sanchez-Molina, I., Chotchuangchutchaval, T., Brown, M., Martinez, L., Rath, T. and Haque, S., 2015. The Role of Oxygen in the Degradation of Methylammonium Lead Trihalide Perovskite Photoactive Layers. *Angewandte Chemie International Edition*, 54(28), pp.8208-8212.
- Bi, D., Yi, C., Luo, J., Décoppet, J., Zhang, F., Zakeeruddin, S., Li, X., Hagfeldt, A. and Grätzel, M., 2016. Polymer-templated nucleation and crystal growth of perovskite films for solar cells with efficiency greater than 21%. *Nature Energy*, 1(10).
- Boix, P., Nonomura, K., Mathews, N. and Mhaisalkar, S., 2014. Current progress and future perspectives for organic/inorganic perovskite solar cells. *Materials Today*, 17(1), pp.16-23.
- Boix, P., Raga, S. and Mathews, N., 2018. Working Principles of Perovskite Solar Cells. *Halide Perovskites*, pp.81-99.
- Cao, J., Yin, J., Yuan, S., Zhao, Y., Li, J. and Zheng, N., 2015. Thiols as interfacial modifiers to enhance the performance and stability of perovskite solar cells. *Nanoscale*, 7(21), pp.9443-9447.
- Castro-Méndez, A., Hidalgo, J. and Correa-Baena, J., 2019. The Role of Grain Boundaries in Perovskite Solar Cells. *Advanced Energy Materials*, 9(38).
- Chan, S., Chang, Y. and Wu, M., 2019. High-Performance Perovskite Solar Cells Based on Low-Temperature Processed Electron Extraction Layer. *Frontiers in Materials*, [e-journal] 6.
- Chaudhary, B., Koh, T., Febriansyah, B., Bruno, A., Mathews, N., Mhaisalkar, S. and Soci, C., 2020. Mixed-Dimensional Naphthylmethylammonium-Methylammonium Lead Iodide Perovskites with Improved Thermal Stability. *Scientific Reports*, 10(1).
- Chen, W., Wu, Y., Yue, Y., Liu, J., Zhang, W., Yang, X., Chen, H., Bi, E., Ashraful, I., Grätzel, M. and Han, L., 2015. Efficient and stable large-area perovskite solar cells with inorganic charge extraction layers. *Science*, 350(6263), pp.944-948.
- Cheng, Y., Xu, X., Xie, Y., Li, H.-W., Qing, J., Ma, C., Lee, C.-S., So, F. and Tsang, S.-W., 2017. 18% High-Efficiency Air-Processed Perovskite Solar Cells Made in a Humid Atmosphere of 70% RH. *Solar RRL*, 1(9), p.1700097.
- Cheng, M., Zuo, C., Wu, Y., Li, Z., Xu, B., Hua, Y. and Ding, L., 2020. Charge-transport layer engineering in perovskite solar cells. *Science Bulletin*, 65(15), pp.1237-1241.

- Conings, B., Drijkoningen, J., Gauquelin, N., Babayigit, A., D'Haen, J., D'Olieslaeger, L., Ethirajan, A., Verbeeck, J., Manca, J., Mosconi, E., Angelis, F. and Boyen, H., 2015. Intrinsic Thermal Instability of Methylammonium Lead Trihalide Perovskite. *Advanced Energy Materials*, 5(15).
- Domanski, K., Correa-Baena, J., Mine, N., Nazeeruddin, M., Abate, A., Saliba, M., Tress, W., Hagfeldt, A. and Grätzel, M., 2016. Not All That Glitters Is Gold: Metal-Migration-Induced Degradation in Perovskite Solar Cells. *ACS Nano*, (6), pp.6306-6314.
- Doosthosseini, F., Behjat, A., Karimi Zarchi, A., Taghavinia, N. and Mirjalili, B., 2020. Photovoltaic parameters and stability study of HTM-free mixed-cation perovskite solar cells by incorporating additives to absorbing layers. *Journal of Materials Science: Materials in Electronics*, 31(9), pp.7123-7132.
- Dualeh, A., Tétreault, N., Moehl, T., Gao, P., Nazeeruddin, M.K. and Grätzel, M., 2014. Effect of Annealing Temperature on Film Morphology of Organic-Inorganic Hybrid Perovskite Solid-State Solar Cells. *Advanced Functional Materials*, 24(21), pp.3250–3258.
- Eperon, G., Stranks, S., Menelaou, C., Johnston, M., Herz, L. and Snaith, H., 2014. Formamidinium lead trihalide: a broadly tunable perovskite for efficient planar heterojunction solar cells. *Energy & Environmental Science*, 7(3).
- Gonzalez-Pedro, V., Juarez-Perez, E., Arsyad, W., Barea, E., Fabregat-Santiago, F., Mora-Sero, I. and Bisquert, J., 2014. General Working Principles of $\text{CH}_3\text{NH}_3\text{PbX}_3$ Perovskite Solar Cells. *Nano Letters*, 14(2), pp.888-893.
- Gosens, I., Post, J., de la Fonteyne, L., Jansen, E., Geus, J., Cassee, F. and de Jong, W., 2010. Impact of agglomeration state of nano- and submicron sized gold particles on pulmonary inflammation. *Particle and Fibre Toxicology*, 7(1).
- Guo, T., Yun, S., Li, Y., Huang, A. and Kang, L., 2020. Magnetron sputtered all-metal-oxide layers with balanced charge carrier transport efficiency for long-term stable perovskite solar cells. *Solar Energy*, 208, pp.652-658.
- Green, M., Dunlop, E., Hohl-Ebinger, J., Yoshita, M., Kopidakis, N. and Hao, X., 2020. Solar cell efficiency tables (version 57). *Progress in Photovoltaics: Research and Applications*, 29(1), pp.3-15.
- Green, M., Ho-Baillie, A. and Snaith, H., 2014. The emergence of perovskite solar cells. *Nature Photonics*, 8(7), pp.506-514.
- Habisreutinger, S., Leijtens, T., Eperon, G., Stranks, S., Nicholas, R. and Snaith, H., 2014. Carbon Nanotube/Polymer Composites as a Highly Stable Hole Collection Layer in Perovskite Solar Cells. *Nano Letters*, 14(10), pp.5561-5568.

Han, T., Lee, J., Choi, C., Tan, S., Lee, C., Zhao, Y., Dai, Z., De Marco, N., Lee, S., Bae, S., Yuan, Y., Lee, H., Huang, Y. and Yang, Y., 2019. Perovskite-polymer composite cross-linker approach for highly-stable and efficient perovskite solar cells. *Nature Communications*, 10(1).

Huang, Z., Wang, D., Wang, S. and Zhang, T., 2018. Highly Efficient and Stable MAPbI₃ Perovskite Solar Cell Induced by Regulated Nucleation and Ostwald Recrystallization. *Materials*, 11(5), p.778.

Icli, K. and Ozenbas, M., 2018. Fully metal oxide charge selective layers for n-i-p perovskite solar cells employing nickel oxide nanoparticles. *Electrochimica Acta*, 263, pp.338-345.

Jena, A., Numata, Y., Ikegami, M. and Miyasaka, T., 2018. Role of spiro-OMeTAD in performance deterioration of perovskite solar cells at high temperature and reuse of the perovskite films to avoid Pb-waste. *Journal of Materials Chemistry A*, 6(5), pp.2219-2230.

Jia, X., Hu, Z., Xu, J., Huang, L., Zhang, J., Zhang, J. and Zhu, Y., 2017. Polymer assisted growth of high-quality perovskite films by Lewis acid-base adduct for efficient planar-heterojunction solar cells. *Materials Research Bulletin*, 95, pp.216–222.

Jordan, D. and Kurtz, S., 2011. Photovoltaic Degradation Rates-an Analytical Review. *Progress in Photovoltaics: Research and Applications*, 21(1), pp.12-29.

Kazmerski, L., 2006. Solar photovoltaics R&D at the tipping point: A 2005 technology overview. *Journal of Electron Spectroscopy and Related Phenomena*, 150(2-3), pp.105-135.

Kim, H., Lee, J., Kim, B., Byun, H.R., Kim, S.H., Oh, H.M., Baik, S. and Jeong, M.S. (2019). Enhanced Stability of MAPbI₃ Perovskite Solar Cells using Poly(p-chloro-xylylene) Encapsulation. *Scientific Reports*, 9(1), pp.1–6.

Kim, S., Bae, S., Lee, S., Cho, K., Lee, K., Kim, H., Park, S., Kwon, G., Ahn, S., Lee, H., Kang, Y., Lee, H. and Kim, D., 2017. Relationship between ion migration and interfacial degradation of CH₃NH₃PbI₃ perovskite solar cells under thermal conditions. *Scientific Reports*, 7(1).

Klein, A., Körber, C., Wachau, A., Säuberlich, F., Gassenbauer, Y., Harvey, S., Proffit, D. and Mason, T., 2010. Transparent Conducting Oxides for Photovoltaics: Manipulation of Fermi Level, Work Function and Energy Band Alignment. *Materials*, 3(11), pp.4892-4914.

Kojima, A., Teshima, K., Shirai, Y. and Miyasaka, T., 2007. Novel Photoelectrochemical Cell with Mesoscopic Electrodes Sensitized by Lead-halide Compounds (5). *ECS Meeting Abstracts*, MA2007-02(8), pp.352-352.

- Kojima, A., Teshima, K., Shirai, Y. and Miyasaka, T., 2009. Organometal Halide Perovskites as Visible-Light Sensitizers for Photovoltaic Cells. *Journal of the American Chemical Society*, 131(17), pp.6050-6051.
- Lan, Y., Wang, Y. and Song, Y., 2020. Efficient flexible perovskite solar cells based on a polymer additive. *Flexible and Printed Electronics*, 5(1).
- Lee, J., Kim, S., Yang, J., Yang, Y. and Park, N., 2019. Verification and mitigation of ion migration in perovskite solar cells. *APL Materials*, 7(4).
- Lei, L., Yang, S., Yu, Y., Li, M., Xie, J., Bao, S., Jin, P. and Huang, A., 2019. Long-term stable perovskite solar cells with room temperature processed metal oxide carrier transporters. *Journal of Materials Chemistry A*, 7(37), pp.21085-21095.
- Leijtens, T., Lauber, B., Eperon, G., Stranks, S. and Snaith, H., 2014. The Importance of Perovskite Pore Filling in Organometal Mixed Halide Sensitized TiO₂-Based Solar Cells. *The Journal of Physical Chemistry Letters*, 5(7), pp.1096-1102.
- Li, J., Dong, Q., Li, N. and Wang, L., 2017. Direct Evidence of Ion Diffusion for the Silver-Electrode-Induced Thermal Degradation of Inverted Perovskite Solar Cells. *Advanced Energy Materials*, 7(14).
- Li, X., Zhang, W., Wang, Y., Zhang, W., Wang, H. and Fang, J., 2018. In-situ cross-linking strategy for efficient and operationally stable methylammonium lead iodide solar cells. *Nature Communications*, 9(1).
- Liu, L., Wang, Z., Sun, W., Zhang, J., Hu, S., Hayat, T., Alsaedi, A. and Tan, Z., 2018. All-solution-processed perovskite light-emitting diodes with all metal oxide transport layers. *Chemical Communications*, 54(94), pp.13283-13286.
- Liu, M., Johnston, M. and Snaith, H., 2013. Efficient planar heterojunction perovskite solar cells by vapour deposition. *Nature*, 501(7467), pp.395-398.
- Liu, X., Wu, T., Chen, J., Meng, X., He, X., Noda, T., Chen, H., Yang, X., Segawa, H., Wang, Y. and Han, L., 2020. Templated growth of FASnI₃ crystals for efficient tin perovskite solar cells. *Energy & Environmental Science*, 13(9), pp.2896-2902.
- Liu, Z., Zhu, A., Cai, F., Tao, L., Zhou, Y., Zhao, Z., Chen, Q., Cheng, Y. and Zhou, H., 2017. Nickel oxide nanoparticles for efficient hole transport in p-i-n and n-i-p perovskite solar cells. *Journal of Materials Chemistry A*, 5(14), pp.6597-6605.
- Marchioro, A., Teuscher, J., Friedrich, D., Kunst, M., van de Krol, R., Moehl, T., Grätzel, M. and Moser, J., 2014. Unravelling the mechanism of photoinduced charge transfer processes in lead iodide perovskite solar cells. *Nature Photonics*, 8(3), pp.250-255.

Mari-Guaita, J., Bouich, A., Shafi, M., Bouich, A. and Mari, B., 2022. Investigation on the Stability and Efficiency of MAPbI₃ and MASnI₃ Thin Films for Solar Cells. *physica status solidi (a)*, 219(5).

Mohammad Bagher, A., 2015. Types of Solar Cells and Application. *American Journal of Optics and Photonics*, 3(5).

Mora-Seró, I., 2018. How Do Perovskite Solar Cells Work?. *Joule*, 2(4), pp.585-587.

Nie, W., Tsai, H., Asadpour, R., Blancon, J., Neukirch, A., Gupta, G., Crochet, J., Chhowalla, M., Tretiak, S., Alam, M., Wang, H. and Mohite, A., 2015. High-efficiency solution-processed perovskite solar cells with millimeter-scale grains. *Science*, 347(6221), pp.522-525.

Ouyang, D., Huang, Z. and Choy, W., 2018. Solution-Processed Metal Oxide Nanocrystals as Carrier Transport Layers in Organic and Perovskite Solar Cells. *Advanced Functional Materials*, 29(1).

Papadas, I., Galatopoulos, F., Armatas, G., Tessler, N. and Choulis, S., 2019. Nanoparticulate Metal Oxide Top Electrode Interface Modification Improves the Thermal Stability of Inverted Perovskite Photovoltaics. *Nanomaterials*, 9(11).

Park, C., Ko, H., Sin, D., Song, K. and Cho, K., 2017. Organometal Halide Perovskite Solar Cells with Improved Thermal Stability via Grain Boundary Passivation Using a Molecular Additive. *Advanced Functional Materials*, 27(42).

Pearson, A., Eperon, G., Hopkinson, P., Habisreutinger, S., Wang, J., Snaith, H. and Greenham, N., 2016. Oxygen Degradation in Mesoporous Al₂O₃/CH₃NH₃PbI_{3-x}Cl_x Perovskite Solar Cells: Kinetics and Mechanisms. *Advanced Energy Materials*, 6(13).

Peng, J., Khan, J., Liu, W., Ugur, E., Duong, T., Wu, Y., Shen, H., Wang, K., Dang, H., Aydin, E., Yang, X., Wan, Y., Weber, K., Catchpole, K., Laquai, F., Wolf, S. and White, T., 2018. A Universal Double-Side Passivation for High Open-Circuit Voltage in Perovskite Solar Cells: Role of Carbonyl Groups in Poly(methyl methacrylate). *Advanced Energy Materials*, 8(30).

Qin, J., Zhang, Z., Shi, W., Liu, Y., Gao, H. and Mao, Y., 2017. The optimum titanium precursor of fabricating TiO₂ compact layer for perovskite solar cells. *Nanoscale Research Letters*, 12(1).

Rhee, S., An, K. and Kang, K., 2020. Recent Advances and Challenges in Halide Perovskite Crystals in Optoelectronic Devices from Solar Cells to Other Applications. *Crystals*, 11(1).

Rong, Y., Hu, Y., Mei, A., Tan, H., Saidaminov, M., Seok, S., McGehee, M., Sargent, E. and Han, H., 2018. Challenges for commercializing perovskite solar cells. *Science*, 361(6408).

Saidaminov, M., Kim, J., Jain, A., Quintero-Bermudez, R., Tan, H., Long, G., Tan, F., Johnston, A., Zhao, Y., Voznyy, O. and Sargent, E., 2018. Suppression of atomic vacancies via incorporation of isovalent small ions to increase the stability of halide perovskite solar cells in ambient air. *Nature Energy*, 3(8), pp.648-654.

Shao, Y., Fang, Y., Li, T., Wang, Q., Dong, Q., Deng, Y., Yuan, Y., Wei, H., Wang, M., Gruverman, A., Shield, J. and Huang, J., 2016. Grain boundary dominated ion migration in polycrystalline organic–inorganic halide perovskite films. *Energy & Environmental Science*, 9(5), pp.1752-1759.

Shi, D., Adinolfi, V., Comin, R., Yuan, M., Alarousu, E., Buin, A., Chen, Y., Hoogland, S., Rothenberger, A., Katsiev, K., Losovyj, Y., Zhang, X., Dowben, P., Mohammed, O., Sargent, E. and Bakr, O., 2015. Low trap-state density and long carrier diffusion in organolead trihalide perovskite single crystals. *Science*, 347(6221), pp.519-522.

Snaith, H., 2018. Present status and future prospects of perovskite photovoltaics. *Nature Materials*, 17(5), pp.372-376.

Soo, Y., Ng, S., Wong, Y. and Ng, C., 2021. Thermal stability enhancement of perovskite MAPbI₃ film at high temperature (150 °C) by PMMA encapsulation. *Journal of Materials Science: Materials in Electronics*.

Soo, Y., Ng, C., Jun, H., Ng, S. and Wong, Y., 2022. Metal oxide sol annealing on perovskite MAPbI₃ film with thermal stability enhanced by caffeine additive and PMMA interlayer. *Journal of Materials Science*, 57(22), pp.10242-10259.

Su, H., Wu, T., Cui, D., Lin, X., Luo, X., Wang, Y. and Han, L., 2020. The Application of Graphene Derivatives in Perovskite Solar Cells. *Small Methods*, 4(10).

Teng, H., Koike, K., Zhou, D., Satoh, Z., Koike, Y. and Okamoto, Y., 2008. High glass transition temperatures of poly(methyl methacrylate) prepared by free radical initiators. *Journal of Polymer Science Part A: Polymer Chemistry*, 47(1), pp.315–317.

Wu, T., Qin, Z., Wang, Y., Wu, Y., Chen, W., Zhang, S., Cai, M., Dai, S., Zhang, J., Liu, J., Zhou, Z., Liu, X., Segawa, H., Tan, H., Tang, Q., Fang, J., Li, Y., Ding, L., Ning, Z., Qi, Y., Zhang, Y. and Han, L., 2021. The Main Progress of Perovskite Solar Cells in 2020–2021. *Nano-Micro Letters*, 13(1).

Xing, G., Mathews, N., Sun, S., Lim, S., Lam, Y., Grätzel, M., Mhaisalkar, S. and Sum, T., 2013. Long-Range Balanced Electron- and Hole-Transport Lengths in Organic-Inorganic CH₃NH₃PbI₃. *Science*, 342(6156), pp.344-347.

- Yang, J., Siempelkamp, B.D., Liu, D. and Kelly, T.L., 2015. Investigation of $\text{CH}_3\text{NH}_3\text{PbI}_3$ Degradation Rates and Mechanisms in Controlled Humidity Environments Using in Situ Techniques. *ACS Nano*, 9(2), pp.1955–1963.
- Yang, H., Zhang, J., Zhang, C., Chang, J., Lin, Z., Chen, D., Xi, H. and Hao, Y., 2017. Effects of Annealing Conditions on Mixed Lead Halide Perovskite Solar Cells and Their Thermal Stability Investigation. *Materials*, 10(7).
- Yin, W., Shi, T. and Yan, Y., 2014. Unique Properties of Halide Perovskites as Possible Origins of the Superior Solar Cell Performance. *Advanced Materials*, 26(27), pp.4653-4658.
- Yoshikawa, K., Kawasaki, H., Yoshida, W., Irie, T., Konishi, K., Nakano, K., Uto, T., Adachi, D., Kanematsu, M., Uzu, H. and Yamamoto, K., 2017. Silicon heterojunction solar cell with interdigitated back contacts for a photoconversion efficiency over 26%. *Nature Energy*, 2(5).
- You, J., Meng, L., Song, T., Guo, T., Yang, Y., Chang, W., Hong, Z., Chen, H., Zhou, H., Chen, Q., Liu, Y., De Marco, N. and Yang, Y., 2015. Improved air stability of perovskite solar cells via solution-processed metal oxide transport layers. *Nature Nanotechnology*, 11(1), pp.75-81.
- Yuan, Y. and Huang, J., 2016. Ion Migration in Organometal Trihalide Perovskite and Its Impact on Photovoltaic Efficiency and Stability. *Accounts of Chemical Research*, 49(2), pp.286-293.
- Zhao, Y., Zhou, W., Han, Z., Yu, D. and Zhao, Q., 2021. Effects of ion migration and improvement strategies for the operational stability of perovskite solar cells. *Physical Chemistry Chemical Physics*, 23(1), pp.94-106.